Title
MRI quantification of cartilage of the knee

Author
Carballido Gamio, Julio

Publication Date
2005

Peer reviewed|Thesis/dissertation

MRI QUANTIFICATION OF CARTILAGE OF THE KNEE

by

Julio Carballido Gamio

DISSERTATION

Submitted in partial satisfaction of the requirements for the degree of

DOCTOR OF PHILOSOPHY

in

Bioengineering

in the

GRADUATE DIVISIONS

of the

UNIVERSITY OF CALIFORNIA SAN FRANCISCO

and

UNIVERSITY OF CALIFORNIA BERKELEY

Date University Librarian

Degree Conferred: .....

This dissertation is dedicated to my parents.

Thanks to all your support I have been able to accomplish this great goal.

Esta tesis está dedicada a mis padres.

Gracias a su apoyo he logrado esta gran meta.

MRI quantification of cartilage of the knee

Julio Carballido Gamio

Abstract

Osteoarthritis (OA) of the knee is a chronic disease that is characterized by degeneration of articular cartilage. Magnetic resonance imaging (MRI) allows the visualization and quantification of this degeneration in vivo. In this dissertation the development of new image processing techniques and application of existing ones to perform inter-subject comparison of knee cartilage thickness are presented. The main characteristic of the proposed method is the registration of cartilage surfaces based on the registration of the corresponding bones. The process is semi-automatic since steps involving segmentation require interaction. Cartilage is segmented using Bezier splines and edge detection, and its shape is then interpolated using a morphing technique to create isotropic voxels. The bones corresponding to the segmented cartilage are segmented with a similar approach and registered based on landmarks. The registration can be rigid-body for intra-subject or elastic for inter-subject comparisons. Landmarks are automatically selected based on shape matching using 3D shape- contexts. Visualization of cartilage thickness maps in three dimensions or overlaid on the MR images is also demonstrated. The cartilage segmentation and the morphing technique were validated visually and based on volumetric measurements of images of porcine knees which cartilage volumes were directly measured using a water displacement method. The registration techniques were validated visually and using manual landmark

registration. Results showed a good agreement between the digital volumetric measurement from the morphed cartilage and the water displacement method with correlation values of 8.3 ($p<0.001$) and 7.5 ($p<0.001$) for 3T and 1.5T, respectively. Registration results also were satisfactory with minimum distances between the registered surfaces of less than the slice thickness. The conclusion was that the proposed image processing techniques were accurate and robust to perform intra-subject and inter-subject comparisons of cartilage thickness of the knee as well as digital volumetric and thickness measurements.

Acknowledgements

With no doubt I am afraid of omitting somebody in this section since there are so many people that I have to acknowledge.

First of all I have to say thanks to my parents. Thanks for the support and encouragement you have given me to accomplish all my goals. I am what I am thanks to you.

Thanks to my brothers. Thanks to your accomplishments and errors my life has been easier.

I also have to say thanks to Dr. Marlene De la Cruz. Thanks for all your help during the admission process to this wonderful Bioengineering program. Your intervention was essential for me to be part of this group and get the Conacyt - UC MEXUS scholarship. I am in debt with you.

Thanks to my research advisor Dr. Sharmila Majumdar, it has been great to be part of your research group. You could not have made easier my adaptation process to the work environment in the US.

Dr. Sarah Nelson and Debra D. Harris also played a key role in my admission to the Bioengineering program. Thanks for making things easier for me as international student. Thanks Debra for helping me to get the Graduate Dean's Health Sciences Fellowship at UCSF.

I cannot forget Dr. Daniel B. Vigneron who was the chair of my qualifying examination. Thanks for your help during this important process.

I also have to say thanks to Dr. Jan S. Bauer for letting me use his data of the porcine cartilage volumes measured by the water displacement method to validate my

segmentation and shape-interpolation techniques; and thanks to Stefanie Krause for segmenting the cartilage of the porcine knees with my programs.

Thanks CONACYT and UC-MEXUS for the scholarship. Please keep helping new students as you helped me.

I have to say thanks to Fulbright for the wonderful experience of being part of this selected group where I was able to meet students from all around the world and know about different cultures.

Thanks to M.S. J.P. Slavinsky for his seminal work on elastic registration to perform inter-subject cartilage knee comparisons and to Serge J. Belongie for the development of the idea of shape-contexts. Both inspired me to do this work.

Finally I have to say thanks to Dr. Duan Xu, thanks for your help, and thanks for collecting the signatures for me while I was away.

This study was supported by NIH grant RO1 AR46905 and RO1 AG17762.

Contents

List of figures

List of tables

Chapter 1
Introduction

1.1 Motivation

Osteoarthritis (OA) is a chronic disease causing deterioration of the joint cartilage. The National Institutes of Health (NIH) in USA estimated that in 2002 more than 20 million people in the United States had OA, and that more than half the population age 65 or older would show x-ray evidence of it in at least one joint. OA affects both men and women, however is more common in men before age 45, and more common in women after age 45. A common manifestation of OA of the knee is the morphological degeneration of articular cartilage. Magnetic resonance imaging (MRI) offers the potential to visualize and analyze quantitatively those changes in vivo [1]. However this quantification and analysis is not straightforward if true 3D analysis is desired. The complications increase when we want to compare the knee cartilage of the same patient at different times, or when we want to compare common regions or points between different patients at any time. These difficulties are the result of anatomical differences, different positioning of patients in the MR scanners, movement of patients during the scans, MR distortions, etc. However, it is important to monitor properly the progression of the cartilage degeneration as well as related treatments. It would also be important to create a reference knee and normalized all other knees to this common framework so comparisons of different properties such as thickness, MR T1 or T2 relaxation times could be performed for different populations in the search of a valid biomarker for OA. In order to accomplish this goal, robust image processing techniques are required.

1.2 Scope of the dissertation

The purpose of this work is to present image processing techniques to perform intra and inter-subject quantification and comparison of knee cartilage morphology. The proposed methodology allows point to point intra and inter-subject comparison of knee cartilage thickness based on the registration of bone structures. After MR image acquisition the process consists of net image processing: cartilage segmentation, interpolation of cartilage based on shape to create isotropic voxels, bone segmentation, image registration based on bone structures, quantification of cartilage thickness and volume, and visualization. This is the evolution of material presented in [2-5].

The developed techniques are demonstrated with examples focused on comparisons of cartilage thickness maps. In order to compare these maps, cartilage is segmented from sagittal MR images of the knee using a semi-automatic segmentation technique based on edge detection and Bezier splines. Because images have highly anisotropic voxels and 3D analysis is desired, shape-based interpolation using a morphing technique is computed to create isotropic voxels representing cartilage. Cartilage volume and thickness is then computed followed by the segmentation of the corresponding bone structures (e.g. femurs for femoral cartilage) by using a similar technique than the employed for cartilage segmentation. This process is applied to the images being compared, and corresponding landmarks are automatically identified in the "source" and "target" segmented bones using 3D shape-contexts. By using rigid-body or non-linear registration algorithms a spatial transformation is then computed based on the identified sets of landmarks and applied to the "source" bone and cartilage surface to align the corresponding structures.

Finally, the registered "source" cartilage is matched to the "target" based on minimum Euclidean distances to establish a point to point correspondence.

It is important to clarify that the objective of this work was the application and development of image processing techniques to perform intra and inter-subject comparison of knee cartilage morphology rather than deduce any characteristics of cartilage changes during arthritic disease progression.

1.3 Dissertation overview

The organization of this dissertation is in the order of the steps just mentioned above. Chapter 2, Background, contains theoretical concepts relevant to understand the contents of the dissertation. Reading of this chapter is suggested for people with no background in MRI or image processing. Although the intention is not to give a full comprehensive review on these topics, it contains enough information to understand the principles behind MRI, image segmentation, interpolation, and image registration. Specific information describing image processing techniques used in following chapters is also included. Chapter 3, Cartilage segmentation, describes the different steps to perform cartilage segmentation. In this chapter the image acquisition parameters are also included together with a brief introduction describing different approaches that have been done to compute segmentation of MRI cartilage of the knee. After cartilage segmentation and before any 3D cartilage quantification and analysis, cartilage shape is interpolated to obtain isotropic voxels. Chapter 4 describes the morphing technique proposed in this dissertation to accomplish this task, as well as a technique to automatically label cartilage surfaces as bone-cartilage interface or articular surface, which is essential to compute 3D

cartilage thickness measurements. A description of the different steps to accomplish shape-based interpolation of cartilage using only distance fields (DFs) and linear interpolation is also presented in Chapter 4. With the creation of cartilage structures represented by isotropic voxels proper 3D analysis can be performed. In Chapter 5 cartilage thickness measurements are introduced as well as different ways to display this information as cartilage thickness maps. Chapter 6 describes two different digital techniques to compute cartilage volume as well as a direct methodology. Chapter 7 is probably the most relevant chapter in this dissertation, since it describes the techniques to accomplish intra and inter-subject registration of cartilage surfaces. So this chapter describes the segmentation of the bone structures to be registered, as well as the automatic landmark identification. Based on the corresponding landmarks affine (rotation, translation, and scaling) and nonlinear transformations are computed and applied to the bone structures as well as to the corresponding cartilage surfaces to perform point to point cartilage thickness comparisons. Chapter 8, Results, presents quantitative and qualitative results validating the segmentation, morphing, and registration techniques. Chapter 9, Discussion, is the last chapter of this dissertation and carefully discusses the advantages and drawbacks of the proposed methodology to perform intra and inter-subject cartilage thickness comparisons. In this chapter future improvements are also proposed to further automate the whole process.

References.

[1] C.G. Peterfy, C. F. van Dijke, D. L. Janzen, C. C. Gluer, R. Namba, S Majumdar, P. Lang, H. K. Genant , "Quantification of articular cartilage in the knee by pulsed saturation and fat-supressed MRI: optimization and validation," *Radiology* 192 (2), pp.485-491, 1994.

[2] J. Carballido-Gamio, T. C. Dunn, G. Lau, S. Banerjee, and S. Majumdar, "Evaluation of a semi-automatic segmentation of cartilage based on K-means," *Proc. ISMRM*, 2003.

[3] E. Ozhinsky and S. Majumdar, "3D Visualization of Cartilage Thickness in Knee Joint Using Bezier Spline Segmentation," *Proc. ISMRM*, 2003.

Chapter 2
Background

2.1 Osteoarthritis of the knee

According to the National Institutes of Health (NIH) of the United States, osteoarthritis (OA) is a chronic disease causing deterioration of the joint cartilage and the formation of new bone (bone spurs) at the margins of the joints. OA is also known as degenerative joint disease or osteoarthrosis, and is the most common type of arthritis, especially among older people. NIH estimated that in 2002 more than 20 million people in the United States had the disease, and that more than half the population age 65 or older would show radiographic evidence of OA in at least one joint. OA affects both men and women, however in men it starts at an earlier age than in woman.

According to the American Academy of Orthopaedic Surgeons, OA of the knee is one of the five leading causes of disability among elderly men and women. The risk for disability from OA of the knee is as great as that from cardiovascular disease. Although OA can affect any joint, the knee is the most common affected site. Fig. 2.1 is a pictorial representation of a normal knee and a knee with OA.

The exact cause of OA is still unknown; however there are some known possible factors such as injury, age, congenital predisposition, and obesity. OA of the knee usually occurs in knees that have experienced trauma, infection or injury.

Articular cartilage is composed of fibrous connective tissue, and has a smooth surface that covers the end of bones to act as a protective cushion or shock absorber in the articulation. When OA of the knee progresses the cartilage thins and the surrounding bones react by becoming thicker. In severe OA cases the cartilage breaks down and its

functionality is lost causing the bones to rub each other and the deformation of the joint. These effects are commonly seen on radiographs as a narrowing of the joint space and osteophytes. Patients with OA of the knee have symptoms such as pain, swelling, and decreased motion.

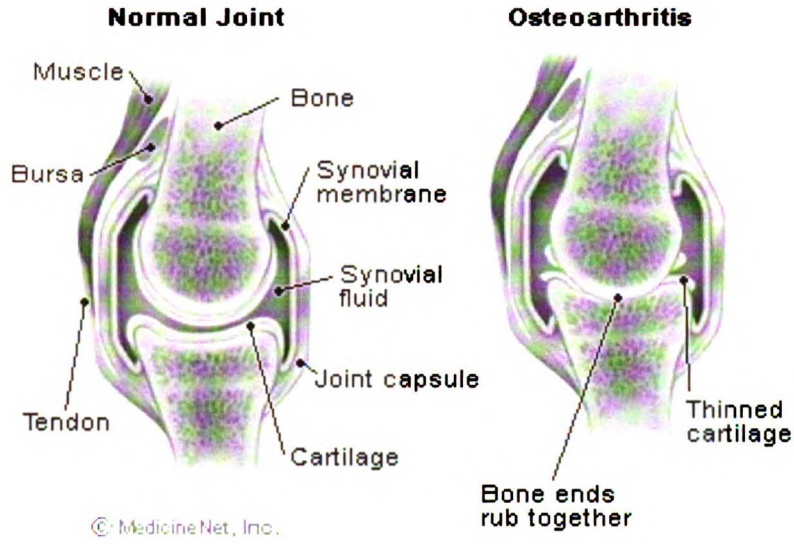

Fig. 2.1 Pictorial representation of a normal knee and a knee with severe OA. Image was taken from http://www.medicinenet.com/osteoarthritis/page2.htm

OA of the knee can be diagnosed based on patient symptoms or based on medical imaging. Patient symptoms include pain and limited functionality in the corresponding knee. The standard medical imaging technique to diagnose OA of the knee is radiography; however MRI has started to play an important role in the characterization of this pathology. MRI allows high spatial resolution images to visualize and quantify cartilage degeneration [1-3], soft tissue abnormalities, and changes in the trabecular bone structure [4-5]. Fig. 2.2 shows an example of a healthy knee joint and one with OA as shown on radiographs, while Fig. 2.3 shows them for a different subject with MRI. As seen in these figures, radiographs offer a good visualization of bone structures, but

cartilage delineation is not possible, while in MRI both cartilage degeneration and internal arrangement of the knee joint are visualized.

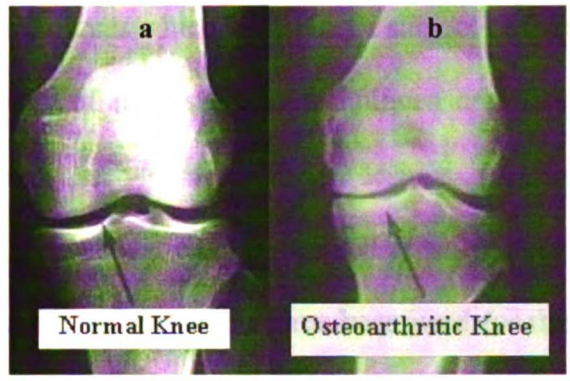

Fig. 2.2 Radiographs of a normal knee (a) and a knee with OA (b). (a) and (b) were taken from: http://www.emedx.com/emedx/diagnosis_information/knee_disorders/knee_osteoarthritis_xrays.htm

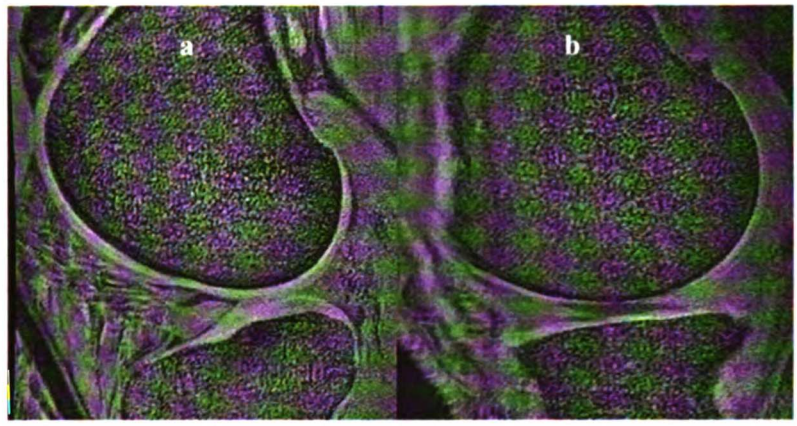

Fig. 2.3 Sagittal 3D fat-suppressed spoiled gradient recalled (SPGR) MR images of a normal knee (a) and a knee with OA (b), where the femoral cartilage has substantially thinned. There is also thinning of the tibial cartilage.

The severity of OA of the knee is usually evaluated using the radiograph based Kellgren-Lawrence (KL) scale [6]: KL scores of 1 and 2 are commonly considered mild OA and classified as OA1; KL scores of 3 and 4 are considered severe OA and classified as OA2; and subjects with no radiographic evidence of OA are classified as OA0.

A wide range of treatments for OA knee are available. Although treatment is tailored to the individual, initial treatment is generally focused to alleviate the pain; however

arthroscopy might be performed to clean bone-cartilage fragments that might cause inflammation and pain. On the other side, total knee replacement (TKR) with insertion of prosthetic devices is considered and end-stage treatment [7]. Intermediate treatments include cartilage repair techniques which have been a subject of intense research over the past few years. A number of new surgical techniques are now available and have revolutionized the therapy of focal cartilage lesions [8-10]. The evolution of osteochondral autograft transplantation has pointed it as one of the most promising techniques [11-17]. A number of synonyms have been used for this technique including mosaicplasty, OATS (osteochondral autograft transfer system) and AOT (autologous osteochondral transplantation). This method is currently considered as the only surgical technique that provides and retains proper hyaline articular cartilage [18]. Cylindrical osteochondral grafts are harvested from the non-weight-bearing area of the proximal femoral condyle and are implanted into joints areas with defective cartilage. This technique is used most frequently at the knee and ankle joints, but has also been advocated in other joints such as the elbow [11]. The main clinical indications for autologous osteochondral transplantation are (i) focal cartilage defects, (ii) osteochondritis dissecans and (iii) osteonecroses.

2.2 Magnetic resonance imaging

Magnetic resonance imaging is a noninvasive imaging modality that involves no ionizing radiation and allows the visualization of soft tissue structures with high contrast and high spatial resolution.

Magnetic resonance originates from the interaction between an atom and an external magnetic field. Atoms with an odd number of protons and/or odd number of neutrons

posses a nuclear spin angular momentum, which make them candidates for MR imaging. These atoms are usually known in the MR community as *spins*.

The nature of MR is based on the interaction of *spins* with three types of magnetic fields: 1) main magnetic field known as B_0, 2) radiofrequency field B_1, and 3) linear gradient fields G.

When *spins* are placed in a magnetic field, they create a net magnetic moment in the direction parallel to the direction of the magnetic field, which is known as the longitudinal direction, and they oscillate at a frequency proportional to its strength, which is known as the *Lamor* frequency and is given by (2.1):

$$\omega_0 = \gamma B_0. \tag{2.1}$$

In (2.1) ω_0 is the *Lamor* frequency; γ is the gyromagnetic ratio, which is a unique constant for each type of atom; and B_0 is the main magnetic field strength. In the presence of a magnetic field *spins* become capable of absorbing energy if they are exposed to electromagnetic energy at the proper frequency of oscillation, in this case the *Lamor* frequency. The magnetic field B_1, which is thousands of times weaker than B_0, is applied to the spins at the *Lamor* frequency in a direction perpendicular to the main magnetic field B_0, promoting an energy absorption as well as a change in the direction of the longitudinal magnetization to the transverse plane to create the transverse magnetization.

When *spins* properly interact with a superposition of linear and perpendicular gradient fields G_x, G_y, G_z, and the B_1 field, each point in space has a unique radio frequency at which the absorbed energy is transmitted as they return to the initial state of equilibrium. Based on the spatial encoding of frequency an image can be created. The strength of the transmitted energy is proportional to the number of *spins* in the tissue. In

biological imaging, hydrogen (^{1}H) is the most abundant *spin*, the most sensitive, and the most studied [19]. The amount of transmitted signal also depends on the local environment of the *spins*. Factors such as mobility and magnetic field homogeneity have a big impact on the final image.

The return of the net magnetization to its original longitudinal orientation is mandated by two relaxation processes:

1) The relaxation back to equilibrium of the component of the nuclear magnetization parallel to B_0 which last time *T1*.
2) The relaxation back to equilibrium of the component of the nuclear magnetization perpendicular to B_0, which last time *T2*.

By proper manipulation of MRI acquisition parameters, images can be "weighted" to accentuate different physical parameters such as proton density, *T1*, *T2*, diffusion, etc.

2.3 Segmentation of MR images.

Image segmentation is the division of an image or volume (stack or sequence of images) into regions that are made up of pixels that have something in common [20]. MRI has become the image modality of interest in the past few years. The large numbers of variables that can be manipulated make MRI a powerful medical imaging device. As other imaging techniques, segmentation of MR images is required to identify anatomic structures, perform intra and inter-modality image registration, and classify functional or pathological areas.

A common segmentation procedure in medical imaging consists of 4 steps as is depicted in Fig. 2.4, where image pre-processing is considered essential in MRI due to the magnetic field inhomogeneities.

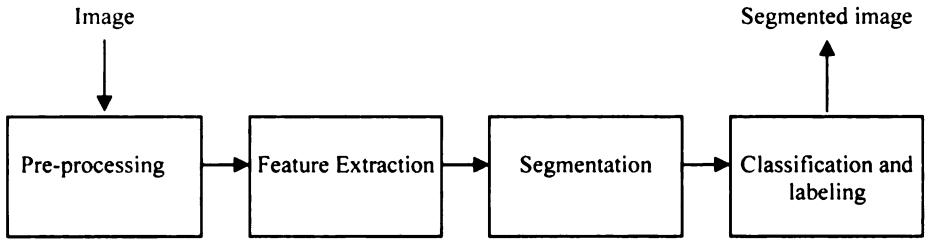

Fig. 2.4. Flow diagram showing the different steps to accomplish successful image segmentation.

a) Image pre-processing: Pre-processing is a crucial step in the segmentation procedure. The main goal in this step is the enhancement of those features that will be used to differentiate the different regions of interest from the rest of the image content. Common enhancement techniques are focused on noise suppression and contrast enhancement. Different methods have been proposed and applied in the MRI community such as linear low pass filtering, wavelet theory, maximum entropy (MEM), expectation maximization (EM), adaptive nonlinear filtering, etc. In this section we will describe three image pre-processing techniques that will be mentioned in Chapter 3 and 7 where cartilage and bone segmentations will be described.

i) Anisotropic diffusion: The primary objective of anisotropic diffusion is to smooth images with no distortion of their edges such that at all scales, intra-region smoothing occurs preferentially over inter-region smoothing [21-22], and to satisfy the causality and immediate localization criteria. In the anisotropic diffusion equation:

$$\mathbf{I}_t = c(x, y, t)\nabla^2\mathbf{I} + \nabla c \cdot \nabla\mathbf{I}, \tag{2.2}$$

where $c(x, y, t)$ is the conduction coefficient, t is the scale variable, ∇ and ∇^2 represent the gradient and Laplacian operators with respect to the space variables, the objective is to assign a value of 1 to the conduction coefficient inside of each region, and 0 at the boundaries.

Setting the conduction coefficient as a function of the magnitude of the gradient of brightness function as suggested by Perona and Malik in [21], provides a good estimate of the edge positions:

$$c(x, y, t) = g(\|\nabla \mathbf{I}(x, y, t)\|), \tag{2.3}$$

where g should be smooth and $g(\cdot)$ is restricted to a subclass of the monotonically decreasing functions. Fig 2.5 shows the function $g(\cdot)$ that was used in this dissertation:

$$e^{-\frac{\|\nabla \mathbf{I}\|}{K}}. \tag{2.4}$$

The anisotropic diffusion algorithm with adiabatic boundary conditions and exponential non-linearity given in [22] was used in this study to increase the brightness homogeneity within the cartilage and bone, while preserving and enhancing the edges. In this function three parameters can be manipulated to control the degree of smoothing and preservation of edges: λ, K, and number of iterations. The parameter λ controls speed of diffusion, and the maximum suggested value is 0.25. The parameter K controls conduction as a function of gradient. Small intensity gradients are able to block conduction and hence diffusion across step edges if K is low. A large value of K reduces the influence of intensity gradients on conduction; and as the number of iterations increases the scale becomes coarser.

ii) Median filtering: The median filter replaces the value of a pixel by the median of the gray levels in the neighborhood of that pixel [23]. The original value of the pixel is included in the computation of the median. The median filter belongs to the class of order statistics filters, that is, filters based on the ordering of the input samples. The median filter is widely known because of its ability to suppress impulse noise while preserving relatively well edge information. It is very efficient in the removal of long-tailed (e.g. Laplacian) noise. However, it is of limited effectiveness in the case of Gaussian noise [24].

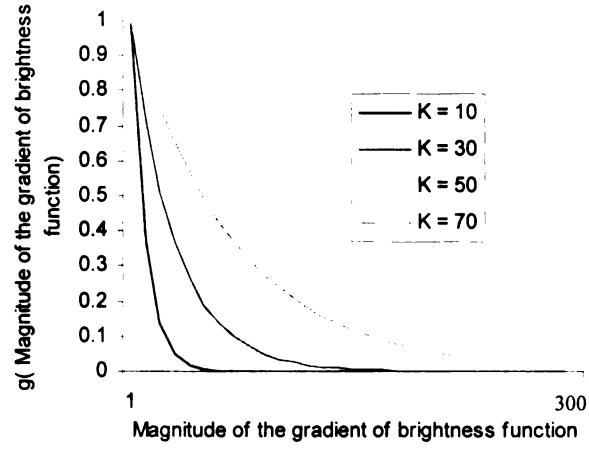

Fig. 2.5. Anisotropic diffusion. Shape of $g(\cdot)$ employed in this dissertation for different values of K.

iii) Power-law transformations: Power-law transformations have the basic form:

$$s = cr^{\gamma} \tag{2.5}$$

where c and γ are positive constants. Power-law transformations with fractional values of γ map a narrow range of dark input values into a wider range of output values, with the opposite being true for higher values of input levels. Power-law transformations with

values of $\gamma>1$ have the opposite effect as those generated with values of $\gamma<1$. Fig. 2.6 shows some plots of equation (2.5) for various values of γ and $c=1$.

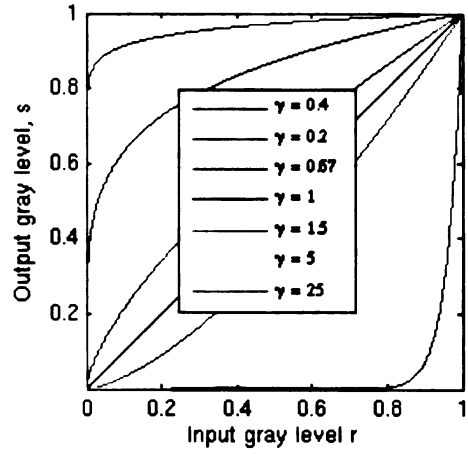

Fig. 2.6. Power-law transformations for different values of γ ($c=1$ in all cases).

b) Feature extraction: Once the image features of interest have been enhanced with image pre-processing techniques they are extracted either automatically or semi-automatically to perform image segmentation. The most common features employed in segmentation of MR images are pixel intensities and edges, however texture and more recently shape have also been utilized.

c) Segmentation: Based on the extracted features the pixels/voxels are grouped together according to different rules of similarity or dissimilarity, shape constraints, statistical models, linguistic rules, etc. Common segmentation algorithms are threshold, edge detection, region growing, clustering, artificial neural networks, snakes, shape models, statistical shape models, geodesic contours, etc. Some segmentation algorithms do not know anything in advance about the object(s) to be segmented, some have *a priori* knowledge of the object such as shape or position, other techniques require training, and

some are performed in 2D or 3D, so segmentation and classification many times are performed together.

Because the main applications of segmented MR images are related with clinical situations, the ideal segmentation techniques are those that are automatic so subjectivity is decreased and reproducibility increased.

There are different segmentation techniques that have been applied to MR images and their applications are strongly related to the image characteristics and the desired region to be segmented. In the following paragraphs a brief description of four common image segmentation techniques is presented:

i) Threshold: This is the simplest method where pixels above certain intensity level are considered the region of interest, and pixels below it are not, or vice versa. There are many different versions of automatic and semi-automatic methods to set proper thresholds based on either global or local information.

ii) Edge detection: Edge detection algorithms usually search for abrupt changes of brightness across the pixel intensity levels. Approximations of derivatives of brightness are commonly used to identify these transitions. Special care has to be taken in the pre-processing step to avoid edge removal or changes of their positions.

iii) Clustering techniques: Segmentation algorithms based on clustering usually group different image features into vectors, that is why they are sometimes called multi-feature or multi-spectral techniques. Then feature vectors are classified based on rules of similarity such as Euclidean distances minimizing iteratively a cost function. K-means clustering and fuzzy c-means are probably the more important segmentation techniques of this type.

iv) Statistical shape-models: The use of shape information to perform segmentation of anatomic structures has become a powerful feature. Segmentation based on shape uses *a priori* knowledge about the expected shape in the image. Usually a set of images are manually segmented to create an average shape of the structure to be segmented. This average shape is represented by a set of eigenvectors and eigenvalues to create what is called the statistical shape model. The average shape is then manually or automatically placed on the image to be segmented, and a deformation process is started guided by the eigenvectors, eigenvalues, and by edge information. The eigenvectors and eigenvalues in the deformation process are commonly called the internal forces, while the edge information is known as the external force.

d) Classification and labeling: This is the final step in an image segmentation procedure and it consists in the recognition of the anatomical structure or functional region that resulted from the corresponding segmentation.

In the literature we can find that many times the segmentation methods are divided as supervised and non-supervised methods. Supervised techniques mean that the operator sets the initial values of the algorithm or simply that there is an interaction of the user with the algorithm performance. Non-supervised algorithms mean that the interaction of the user is minimized, and the final result is almost/or operator independent.

2.4 Interpolation

According to [25] interpolation is "model-based recovery of continuous data from discrete data within a known range of abscissas". Interpolation is almost never the goal in itself; however its applications in medical imaging are numerous. Probably the most

common application in MRI is related to the creation of isotropic images. In MRI there is a trade-off between SNR and image resolution, and with current technology good quality isotropic MR images of the knee are not possible yet. So the in-plane resolution is many times higher than the through plane resolution resulting in highly anisotropic voxels. If proper visualization or 3D analysis of anatomic structures is desired, then isotropic voxels should be created. Gray-level and shape-based interpolation are the two main interpolation categories and different papers have been published to approach this common problem in image analysis and display [26-36].

2.4.1 Gray level interpolation

Nearest neighbor, linear, and cubic interpolation are the three most known gray-level interpolation methods. The simplest and most efficient method from the implementation point of view is nearest neighbor. This method, which is also called *zero-order interpolation*, assigns to the interpolated voxel the gray-level of the closest non-interpolated one. This technique often produces undesirable artifacts such as distortion of straight edges in high-resolution images [23]. Smoother results can be obtained with *cubic convolution interpolation*, which is an interpolation technique that fits a surface of the $\sin(z)/z$ type through a much larger number of neighbors in order to obtain a smooth estimate of the gray level at any desired point [23]. However this technique is considered computational expensive and usually is replaced by linear interpolation techniques (bi-linear and tri-linear for 2D and 3D images, respectively) which give satisfactory results at a lower computational cost. Linear interpolation of gray levels consists in linearly interpolating points within a square (2D) or box (3D) given the values at the vertices.

2.4.2 Shape-based interpolation

Many times the extraction of the shape of a 3D structure from the MR image is required for its subsequent quantification and analysis. When working with images with anisotropic voxels there are two possible approaches to deal with these cases and perform proper 3D analysis: 1) perform gray-level interpolation to obtain a new gray-level image with isotropic voxels and then segment the volume of interest, or 2) segment the structure of interest and interpolate the shape of this structure to obtain isotropic voxels. Both methods are valid, however when totally automatic segmentation approaches cannot be implemented, the first approach has the drawback of increasing the number of slices that the user has to interact with to segment the structure of interest. This factor could be up to ten times the initial number of slices. So a segmentation of a structure which originally was contained in 40-60 slices has increased to a segmentation of 400-600 slices. When dealing with manual segmentation techniques, this makes the gray-level approach undesirable.

There are different approaches to interpolate shape. However, there are probably three main categories: 1) those based on distance fields (DFs) [26-28]; 2) those based on morphological operations [29-34]; and 3) those based on morphing [35-39].

Morphological techniques represent the shapes of the images to be interpolated as binary structures. Then with a combination of erosion and dilation operations the new shapes are interpolated. The disadvantage of these techniques is that they have difficulty in interpolating shapes which are represented by few pixels since the erosion operations, which are not reversible, sometimes eliminate structures of interest.

Distance field interpolation has become the shape-based interpolation of choice. This technique represents the shapes to be interpolated as DFs. The pixel values of the images to be interpolated are replaced by their distances to the closest object contour. Distance values inside or on the contour have different sign than those outside. Then by using linear or cubic interpolation, DFs are interpolated and the new object is extracted from the interpolated DF based on pixel signs.

Morphing interpolates shape based on DFs and warping. Morphing or image metamorphosis is a well known tool in the animation and visual effects community. Morphing is commonly used to create smooth transitions between digital images giving a blending sensation. Morphing of two images into an intermediate one is commonly accomplished with a three step process:

1) *Feature Correspondence*: Feature correspondence between the images is performed based on pairs of feature primitives such as points or lines. In animation this step, which is considered crucial to generate satisfactory results, is commonly done manually although automatic techniques are available.

2) *Warping*: Intermediate features are generated and a mapping function which is generally non-linear is computed to map the sets of features of both images onto the intermediate set. The mapping function, also know as warping is then applied to all points in both images.

3) *Image interpolation*: Color blending also known as cross-dissolve is performed on the warped images to create the morphed in between one. In our application these images were the corresponding warped DFs as done in [35].

The current technique that is considered the standard for cartilage interpolation is that proposed in [41]. This technique interpolates shape based only on DFs, can handle branching, and its robustness has been demonstrated. The interpolation technique that will be presented in Chapter 4 is a morphing technique. The main reason behind this election was that morphing is better at handling situations of objects with invaginations [35] that can occur in cases such as cartilage lesions. A comparison of both methodologies will also be presented.

2.5 Shape matching

Point matching between two shapes is a common problem in medical image processing techniques such as registration. "Image registration is the problem of finding a spatial transformation mapping an object in one image to a similar object in another image. When this problem is solved using shape information from the two objects, it is referred to as shape matching" [42]. Point-based shape matching refers when the shape is represented by points. These points could be points of high curvature, edges, specific patterns such as endpoints, etc. In [43] Belongie et al suggested to extract shape features along the edges of each object, determine pairs of corresponding shape features, and then by using the correspondence information find an optimal aligning transformation. They also suggested performing the second and third steps iteratively.

2.5.1 Shape-contexts

In [44] we presented and validated a 3D automatic point matching technique applied to medical imaging. The technique was an extension to 3D of the work presented in [43]

and it was also independently developed in [45]. Point matching is accomplished based on 3D descriptors called shape-contexts that characterize the shape of each point based on histograms of the distribution of points around them. Corresponding points on similar shapes will have similar shape-contexts. In comparison to other point matching techniques, shape-contexts do not require equal number of points for the shapes to be compared or segments with high curvature. 3D shape-contexts are histograms computed in 3D log-polar spaces (r, θ, and φ) on points defining the shape surface, are invariant to translation, and can be invariant to scale and rotation. An example of a bin in a 3D shape-context is shown in red in Fig. 2.7a. An image representation of a 3D shape-context for a control point of a spline representing the shape of a tibia is shown in Fig. 2.7b with a total of 1183 bins (7 values for r, 13 values for θ, and 13 values for φ). For this example only the control points of the splines defining the bone shape were considered. Fig. 2.7c shows the shape-descriptor in 2D for reference purposes, which could be considered the cross-section at the equator of a shape-context in 3D.

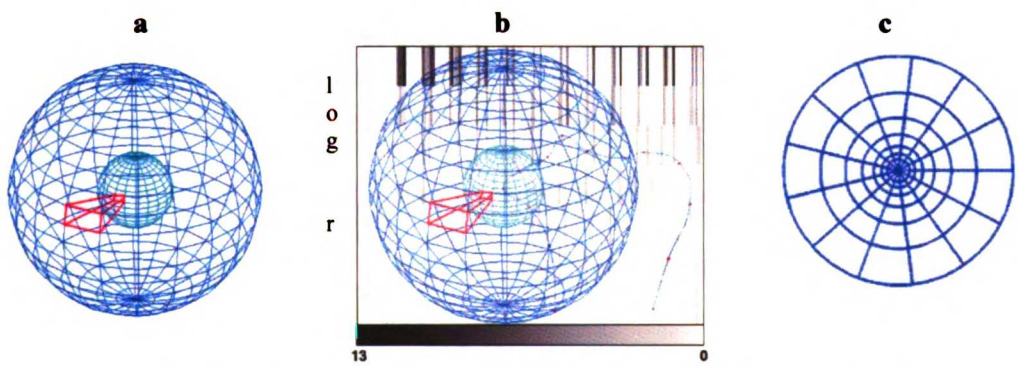

Fig. 2.7. (a) 3D shape-context with a bin highlighted in red. This shape-context is only representing the 2 most inner radial sections of the 3D polar histogram structure. (b) Image representation of a 3D polar histogram obtained using a 3D shape-context for a control point of a spline defining the shape of a tibia. The vertical axis corresponds to the radial sections (7 for this example); while the horizontal axis represent the bins at different angles (169 angles for this example; 13 values for θ, and 13 values for φ). (c) 2D shape-context with a total of 91 bins (7 values for r, and 13 values for θ).

2.5.2 Point matching

In order to match two shapes their corresponding 3D shape-contexts are compared to each other based on the χ^2 test statistic (2.6), a simple and effective measure of histogram similarity:

$$\chi^2(h_i, h_j) = \frac{1}{2}\sum_{v=1}^{V}\frac{(h_i(v) - h_j(v))^2}{h_i(v) + h_j(v)}, \tag{2.6}$$

where V is the total number of bins in the histograms (shape-contexts), $h_i(v)$ the number of points inside the vth bin of the ith local histogram, and same idea for $h_j(v)$. The output of this statistic could be considered as the cost of matching the points of the shape-contexts under evaluation [43].

Once all the pair-wise costs are computed, a 1-to-1 point matching that minimizes the total cost is required. The optimal point matching in [44] was solved by using the Hungarian method [46]. However in this work we used the robust contour matching technique via the order preserving assignment problem (COPAP) [42], which minimizes the total cost of this assignment, satisfies the criterion of 1-to-1 matching, allows the matching of only a fraction of points to increase robustness with respect to shape irregularity, and avoids the crossing of landmarks which is physically implausible. Although the latter characteristic was intended for 2D contour matching, its extension to 3D was straightforward for our application since we had an ordered set of points in 3D.

2.6 Image registration

"The goal of image registration is to determine a spatial transformation that will bring homologous points in images being registered into correspondence" [47]. There are two main categories of image registration techniques: feature-based and direct. Feature-based

methods use manually or automatically selected features and minimize a cost function which objective is to align them. Direct methods used the pixel intensities themselves to perform this alignment.

Based on the minimization of cost functions there are different transformations that manipulate the coordinates of the "source" image to match those of the "target". It is common to classify these transformations according to their degrees of freedom (DOF), which are the number of independent ways that the transformation can be changed. Rigid-body transformations refer to those transformations that could be applied to a solid structure: rotations and translations. Rigid body transformations have 6 DOF. The next level of transformation is affine which incorporates scaling and shear giving us 12 DOF. Elastic or non-linear transformations have from 12 to millions DOF.

2.6.1 Affine Registration

The affine transformation in this paper was accomplished by using [48]. In [48] Horn et al solve what they call in photogrammetry the absolute orientation problem of two 3D point sets. Given a set of corresponding landmarks for the source and target shapes, Horn gives a closed form solution to find the optimal rotation (R), translation (r_o), and scale (s) that maps the set of N source landmarks (l_S) onto the target set (l_T):

$$. l_T = s R l_S + r_o . \tag{2.7}$$

The solution proposed by Horn minimizes the sum of the squared distances between the set of landmarks:

$$\sum_i^N \|e_i\|^2, \tag{2.8}$$

where e_i is given by (2.9):

$$e_i = l_{T,i} - s\,R(l_{S,i}) - r_o. \tag{2.9}$$

2.6.2 Elastic registration

Elastic registration in this work was accomplished by using Wendland's radial basis functions (RBFs) [49] as proposed by Fornefett et al. in [50]. These RBFs have compact support, are positive definite, constructed from piecewise polynomials, and of the following general form:

$$\psi(r) = \begin{cases} p(r) & 0 \le r \le 1 \\ 0 & r > 1 \end{cases} \tag{2.10}$$

where $p(r)$ is a univariate polynomial. For a specified space dimension $d > 0$ and smoothness parameter $k \geq 0$ there exists a unique Wendland function $\psi_{d,k}(r) \in C^{2k}(\mathbb{R})$ which is positive definite on $\mathbb{R}^d$ and has a polynomial of minimal degree $floor(d/2) + 3k + 1$, where $floor(x)$ returns the largest integer $\le x$. In this work the selected function was:

$$\psi_{3,1}(r) = (1-r)_+^4 (4r+1), \tag{2.11}$$

where

$$(1-r)_+^u = \begin{cases} (1-r)^u & 0 \le r \le 1 \\ 0 & else \end{cases}. \tag{2.12}$$

The selection was based on [50] where Fornefett chose the pair $(d, k) = (3, 1)$ as it gave the smallest degree polynomial that was still smooth and differentiable when evaluated at $r = 0$. The mathematical properties also hold for different spatial supports a beyond unity:

$$\psi_a(r) = \psi(r/a). \tag{2.13}$$

For (2.11) Fornefett et al. suggested in [50] a minimum value of a equal to 2.98 the

maximum landmark displacement for 2D, and 3.66 the maximum landmark displacement for 3D.

References.

[1] C.G. Peterfy, C. F. van Dijke, D. L. Janzen, C. C. Gluer, R. Namba, S Majumdar, P. Lang, H. K. Genant , "Quantification of articular cartilage in the knee by pulsed saturation and fat-supressed MRI: optimization and validation," *Radiology* 192 (2), pp.485-491, 1994.

[2] T.C. Dunn TC, Y. Lu , H. Jin, M.D. Ries, S. Majumdar, "T2 relaxation time of cartilage at MR imaging: comparison with severity of knee osteoarthritis," *Radiology*, vol. 232, no. 2, pp. 592-598, 2004.

[3] K.Y. Lee, T.C. Dunn, L.S. Steinbach, E. Ozhinsky, M.D. Ries, S. Majumdar, "Computer-aided quantification of focal cartilage lesions of osteoarthritic knee using MRI," *Magnetic Resonance Imaging*, vol. 22, no. 8, pp. 1105-1115, 2004.

[4] C.T. Lindsey, A. Narasimhan, J.M. Adolfo, H. Jin, L.S. Steinbach, T. Link, M. Ries, S, Majumdar, "Magnetic resonance evaluation of the interrelationship between articular cartilage and trabecular bone of the osteoarthritic knee," *Osteoarthritis and Cartilage*, . Feb;12 (2), pp. 86-96, 2004..

[5] G. Blumenkrantz, C.T. Lindsey, T.C. Dunn, H. Jin, M.D. Ries, T.M. Link, L.S. Steinbach, S. Majumdar, "A pilot, two-year longitudinal study of the interrelationship between trabecular bone and articular cartilage in the osteoarthritic knee," *Osteoarthritis and Cartilage*, Dec; 12 (12), pp. 997-1005, 2004.

[6] J. Kellgren, J. Lawrence, "Radiologic assessment of osteoarthritis," *Ann. Rheum. Dis.*, 16:494-502, 1957.

[7] S. Gosh, "Magnetic resonance imaging based evaluation of articular cartilage degeneration in osteoarthritis of the knee," Ph.D. Dissertation, *University of California San Francisco, University of California Berkeley*, 2001.

[8] D. Koulalis, W. Schultz, M. Heyden, F. Konig, "Autologous osteochondral grafts in the treatment of cartilage defects of the knee joint," *Knee Surg Sports Traumatol Arthrosc*, 12:329-334, 2004.

[9] G. Bentley, L.C. Biant, R.W. Carrington, M. Akmal, A. Goldberg, A.M. Williams, J.A. Skinner, J. Pringle, "A prospective, randomised comparison of autologous chondrocyte implantation versus mosaicplasty for osteochondral defects in the knee," *J Bone Joint Surg*, Br 85:223-230, 2003.

[10] E.L. Cain, W.G. Clancy, "Treatment algorithm for osteochondral injuries of the knee," *Clin Sports Med*, 20:321-342, 2001.

[11] A.B. Imhoff, G.M. Ottl, A. Burkart, S. Traub. "Osteochondrale autologe Transplantation an verschiedenen Gelenken," *Orthopade*, 28:33-44, 1999.

[12] A.B. Imhoff, G.M. Oettl, "Arthroscopic and Open Techniques for Transplantation of Osteochondral Autografts and Allografts in Various Joints," *Surg Technol Int*, VIII:249-252, 2000.

[13] R.P. Jakob, T. Franz , E. Gautier, P. Mainil-Varlet, "Autologous osteochondral grafting in the knee: indication, results, and reflections," *Clin Orthop*, 170-184, 2002.

[14] L. Hangody, P. Fules, "Autologous osteochondral mosaicplasty for the treatment of full-thickness defects of weight-bearing joints: ten years of experimental and clinical experience," *J Bone Joint Surg Am*, 85-A Suppl 2:25-32, 2003.

[15] L. Hangody, "The mosaicplasty technique for osteochondral lesions of the talus," *Foot Ankle Clin*, 8:259-273, 2003.

[16] L. Hangody, G.K. Rathonyi, Z. Duska, G. Vasarhelyi, P. Fules, L. Modis, "Autologous osteochondral mosaicplasty. Surgical technique," *J Bone Joint Surg Am* 86-A Suppl 1:65-72, 2004.

[17] G. Kish, L. Modis, L. Hangody, "Osteochondral mosaicplasty for the treatment of focal chondral and osteochondral lesions of the knee and talus in the athlete. Rationale, indications, techniques, and results," *Clin Sports Med* 18:45-66, vi, 1999.

[18] P. Ueblacker, A. Burkart, A.B. Imhoff, "Retrograde cartilage transplantation on the proximal and distal tibia," *Arthroscopy*, 20:73-78, 2004.

[19] D.G. Nishimura, "Principles of Magnetic Resonance Imaging".

[20] Maria Petrou. Image Processing. The Fundamentals, pp. 265.

[21] P. Perona and J. Malik, "Scale-space and edge detection using anisotropic diffusion," *IEEE Ttrans. PAMI*, vol. 12, issue 7, pp. 629-639, July 1990.

[22] P. Perona, T. Shiota, and J. Malik, "Anisotropic diffusion," in Geometry-*Driven Diffusion in Computer Vision*, vol. 1., pp. 73-92, 1994.

[23] R.C. Gonzalez, R.E. Woods, "Digital Image Processing," *Prentice Hall*, 2nd edition.

[24] N. Nikolaidis, I. Pitas, "3-D Image Processing Algorithms," *John Wiley & Sons, Inc.*

[25] P. Thévenaz, T. Blu, and M. Unser, "Image Interpolation and Resampling," in *Handbook of Medical Imaging, Processing and Analysis.*

[26] D. Levin, "Multidimensional Reconstruction by Set-valued Approximation," *IMA J. Numerical Analysis*, 6:173-184, 1986.

[27] S.P. Raya and J. K. Udupa, "Shape-Based Interpolation of Multidimensional Objects, " *IEEE Transactions on Medical Imaging*, vol. 9, no. 1, March 1990.

[28] G. J. Grevera, J. K. Udupa. "Shape-Based Interpolation of Multidimensional Grey-Level Images," *IEEE Transactions on Medical Imaging*, vol. 15, no. 6, December 1996.

[29] G. T. Herman, J. Zheng, C. A. Bucholtz, "Shape-based interpolation," *IEEE Computer Graphics and Applications* 12(3):69-79, 1992.

[30] J.-F. Guo, Y.-L. Cai, and Y.-P. Wang, "Morphology-based interpolation for 3D medical image reconslruction," *Cornput. Meal. Imaging Graph.*, vol. 19, no. 3, pp. 267 279, 1995.

[31] B. Migeon, R. Charreyron, P. Deforge, P. Marché, "Improvement of morphology-based interpolation," *Proc. of the 20th Annual International Conference of the IEEE EMBS*, vol. 20, no. 2, 1998.

[32] Tong-Yee Lee and Wen-Hsiu Wang. "Morphology-Based Three-Dimensional Interpolation," *IEEE Transactions on Medical Imaging*, vol. 19, no. 7, July 2000.
[33] Vassilios Chatzis and Ioannis Pitas. "Interpolation of 3-D Binary Images Based on Morphological Skeletonization," *IEEE Transactions on Medical Imagining*, vol. 19, no. 7, July 2000.
[34] A. G. Bors, L. Kechagias, and I. Pitas. "Binary Morphological Shape-Based Interpolation Applied to 3-D Tooth Reconstruction," *IEEE Transactions on Medical Imaging*, vol. 21, no. 2, February 2002.
[35] Tong-Yee Lee and Chao-Hung Lin. "Feature-Guided Shape-Based Image Interpolation," *IEEE Transactions on Medical Imaging*, vol. 21, no. 12, December 2002.
[36] T. Beier, and S. Neely, "Feature-Based Image Metamorphosis," *Computer Graphics*, 26, 2, July 1992.
[37] D. Cohen-Or, D. Levin, A. Solomovici, "Contour Blending Using Warp-Guided Distance Field Interpolation," *Proc. IEEE Visualization*, 1996.
[38] H. Johan, Y. Koiso, T. Nishita, "Morphing Using Curves and Shape Interpolation Techniques," *Proc. Pacific Graphics*, 2000.
[39] D. Cohen-Or, D. Levin, A. Solomovici, "Three-Dimensional Distance Field Metamorphosis," *ACM Transactions on Graphics*, vol. 17, no. 2, pp. 116-141, 1998.
[40] B. Migeon, R. Charreyron, P. Deforge, A. Langlet, J. Renard, P. Marche, "An automatic spline-based contour interpolation for the 3D reconstruction of a thin walled elastic tube," *Journal of Biomechanics* 31 (1001) (1998) pp. 70-70.
[41] T. Stammberger, F. Eckstein, K. Englmeier, M. Reiser, "Determination of 3D Cartilage Thickness Data From MR Imaging: Computational Method and Reproducibility in the Living," *Magnetic Resonance in Medicine*, 41:529-536(1999).
[42] C. Scott and R. Nowak, "Robust Contour Matching via the Order Preserving Assignment Problem," submitted. Available at:*http://www.stat.rice.edu/~cscott/pubs.html*. Unpublished.
[43] S. Belongie, J. Malik, and J. Puzicha, "Shape Matching and Object Recognition Using Shape Contexts," IEEE Trans.PAMI, vol. 24, no. 24, 2002.
[44] J. Carballido-Gamio, K-Y Lee, S. Majumdar, "Automatic 3D point matching of segmented images using shape-contexts," *Proc. ISMRM*, 2005.
[45] A. Frome, D. Huber, R. Kolluri, T. Bülow, and J. Malik, "Recognizing Objects in Range Data Using Regional Point Descriptors," European Conf. on Computer Vision, 2004.
[46] Niclas Borlin, Dept. of Computing Science, Ume University, Sweden.
[47] Roger P. Woods, "Registration," in *Handbook of Medical Imaging, Processing and Analysis*.
[48] B.K.P. Horn, H.M. Hilden, S. Negahdaripour, "Closed-from solution of absolute orientation using orthonormal matrices," *J. Opt. Soc. Am. A.*, vol. 5, no. 7, 1988.
[49] H. Wendland, "Piecewise polynomial, positive definite and compactly supported radial basis functions of minimal degree," *Adv. Comput. Math.*, vol. 4, pp. 389-396, 1995.
[50] M. Fornefett, K. Rohr, H.S. Stiehl, "Radial basis functions with compact support for elastic registration of medical images," *Image and Vision Computing*, 19, pp. 87-96, 2001.

Chapter 3
Cartilage segmentation

Automatic [1] and semi-automatic [2-7] approaches to segment cartilage of the knee from MR images have been published after the generation of high resolution and high contrast images obtained with 3D spoiled gradient recalled (SPGR) fat suppressed pulse sequences. Because these images offer good contrast at the bone-cartilage interface (bone=dark, cartilage=bright), many methods based on edge detection have been explored and validated [3-5, 7]. However, the segmentation task is still time consuming and the amount of human interaction is considerable due to the common noisy characteristics of MR images of patients with osteoarthritis (OA). So with the aim of reducing the time and effort of manual segmentation while preserving accuracy, a semi-automatic, interactive segmentation technique that is based on edge-detection and Bezier spline interpolation was developed. The segmentation technique is the evolution of material presented in [6-7].

3.1 Image acquisition

3.1.1 In vitro

Sagittal MR images of 12 and 16 fresh porcine knees were obtained at 1.5T and 3T (Signa, General Electric, Milwaukee, WI), respectively, using a quadrature knee coil. The porcine knees were stored at -80°C between the measurements, and thawed to room temperature in a water quench for imaging. At 1.5 T images were acquired with a 3D SPGR pulse sequence. At 3T images were acquired with a 3D water excitation spoiled gradient echo sequence (WE). All porcine images were acquired with fat suppression and in-plane resolution of 0.195mm x 0.195mm after reconstruction. Table 3.1 and Table 3.2

show the image acquisition parameters [8], while. Fig. 3.1 and Fig. 3.2 show representative images for the porcine knees at 1.5T and 3T, respectively.

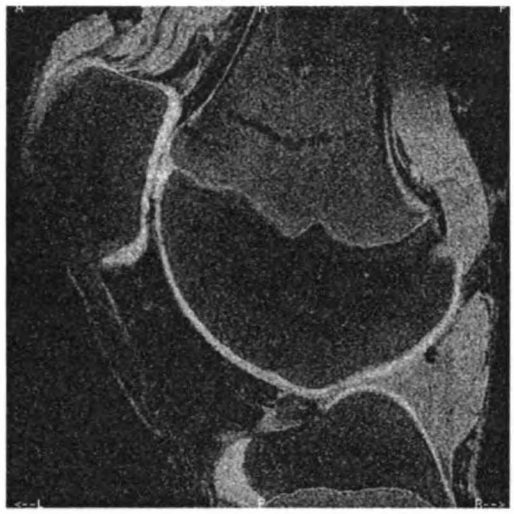

Table 3.1. MR image acquisition parameters for porcine knees at 1.5T.	
Pulse sequence	*3D SPGR*
TR (ms)	27.5
TE (ms)	7.5
Flip angle (°)	20
BW (kHz)	31.25
Imaging time (min)	5:38
Matrix	512 x 512
NEX	1
Slice thickness (mm)	1.5
Number of slices	48

Fig. 3.1. Representative SPGR image of a porcine knee at 1.5T.

The rationale behind the images of porcine knees was the idea of validating the current cartilage manual segmentation technique [9] used in our OA studies [10-12], comparing the digital volume measurements to those obtained directly from scrapped cartilage using a water displacement method [8] (see Chapter 6 for more details). This idea was then extended to validate the semi-automatic segmentation technique proposed in Section 3.2.

3.1.2 In vivo

In vivo sagittal MR images of 5 human knees of subjects with different levels of OA (2 OA0, 2 OA1, 1 OA2) were also acquired at 1.5T (Signa, General Electric, Milwaukee, WI) using a 3D fat-suppressed SPGR sequence and a bilateral dual-phased array coil (USA Instruments, Cleveland, OH). Subjects were positioned supine in the scanner, and the knee to be imaged was secured using a knee-holder (constructed in-house) that

allowed the knee to flex 30° ± 1°. The receiver coils were secured to and centered at the knee joint, so that signal to noise ratio was maximized. Images were acquired with fat suppression and in-plane resolution of 0.234mm x 0.234mm after reconstruction. Table 3.3 shows a list of the image acquisition parameters while Fig. 3.3 shows a representative image.

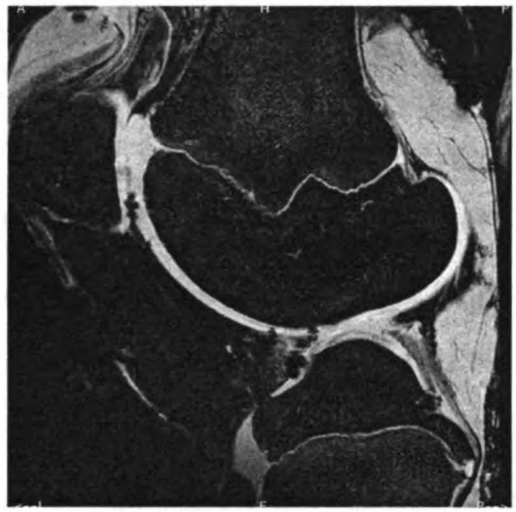

Table 3.2. MR image acquisition parameters for porcine knees at 3T.

Pulse sequence	*3D WE*
TR (ms)	27.5
TE (ms)	13.12
Flip angle (°)	12
BW (kHz)	15.63
Imaging time (min)	5:38
Matrix	512 x 512
NEX	1
Slice thickness (mm)	1.5
Number of slices	48

Fig. 3.2. Representative WE image of a porcine knee at 3T.

Table 3.3. MR image acquisition parameters for human knees at 1.5T.

Pulse sequence	*3D SPGR*
TR (ms)	30
TE (ms)	3.3
TI(ms)	8
Flip angle (°)	30
Imaging time (min)	9:31
Matrix	512 x 512
NEX	1
Slice thickness (mm)	2
Number of slices	60

Fig. 3.3. Representative fat-suppressed SPGR image of a human knee at 1.5T.

To correct for non-uniform signal intensity 3D low pass filtering was applied to all in-vivo acquisitions [13].

3.2 Sagittal semi-automatic segmentation of cartilage

Cartilage was segmented from sagittal MR images of porcine and human knees by using a semi-automatic segmentation technique based on Bezier splines and edge-detection. The user placed control points inside the cartilage (e.g. femoral cartilage) following its shape to create a Bezier spline as is shown in Fig. 3.4a. All splines were placed counter-clockwise (with the center of the clock in the corresponding bone) and the end points remained in their original positions during the segmentation process. Then, based on the maximum and minimum x and y coordinates of the splines, a bounding box with an extra frame of 30 pixels was created to speed up the segmentation process, and the new sub-image was normalized against its maximum gray level value.

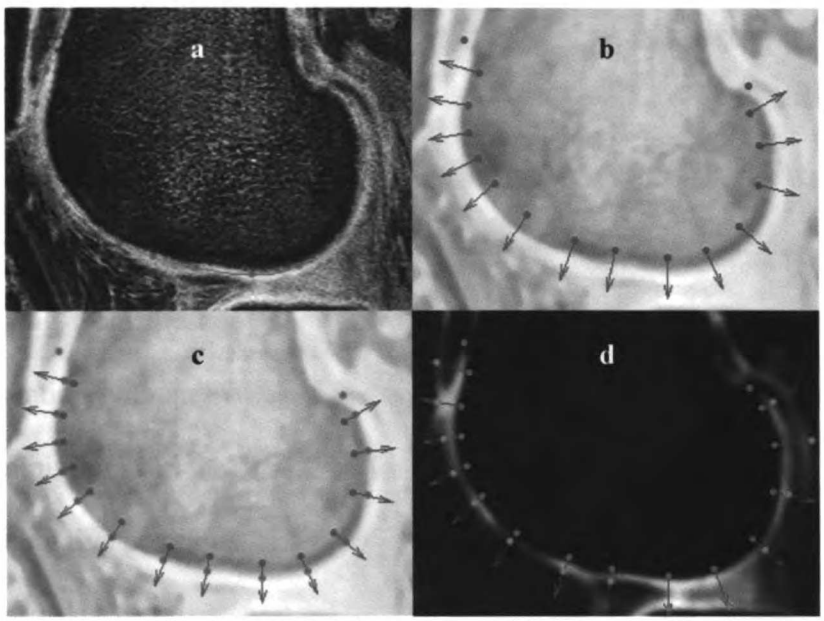

Fig. 3.4. (a) Initial spline defining the shape of the femoral cartilage to be segmented is shown in green with its corresponding control points for a human knee. (b) Line profiles used to find the bone-cartilage interface are shown with blue arrows. (c) Green points representing the bone-cartilage interface at the line profiles. (d) New line profiles are shown with blue arrows, and tentative positions for the articular surface at the line profiles are shown with red points. Note the different image pre-processing in (c) and (d).

In order to find the bone-cartilage interface, which was considered to be detected with more confidence than the articular surface because of the high contrast offered by the fat suppressed images (bone=dark, cartilage=bright), the image edges were enhanced using an anisotropic diffusion algorithm [14] (λ=0.25, *number of iterations*=5, K=90) and a median filter (7 pixels x 7 pixels), followed by a contrast enhancement technique based on a power law transformation [15] (c=1, γ=1/3). Then rays perpendicular to the splines on the control points were traced towards the bone-cartilage interface to a distance equal to a width of 15 pixels. From these positions, line profiles were computed back to the cartilage using bicubic interpolation with an average of two points per pixel (Fig. 3.4b) for a total of 60 points (~30 pixels). After computing the first derivative of brightness of the line profiles, the maximum value of the first 30 points was taken as the bone-cartilage interface for each point (Fig. 3.4c).

The original sub-image was taken again, smoothed with an anisotropic diffusion algorithm (λ=0.25, *number of iterations*=20, K=9), and contrast enhanced by a power law transformation (c=1, γ=3) to find the articular surface. No median filtering was applied this time. Starting from the bone-cartilage interface, line profiles were computed using bicubic interpolation with an average of two points per pixel for a total of 60 points (~30 pixels). The minimums of the first derivatives of brightness of the line profiles were considered as tentative positions for the articular surface (Fig. 3.4d).

New line profiles were computed in opposite direction of those shown in Fig. 3.4b using the new pre-processed sub-image as is shown in Fig. 3.5a. Using the maximums of the first derivatives of brightness of the first 30 points, different tentative positions for the

articular surface were found (Fig. 3.5b). Using the minimums of the first derivatives of brightness, new points for the bone-cartilage interface were found (Fig. 3.5c).

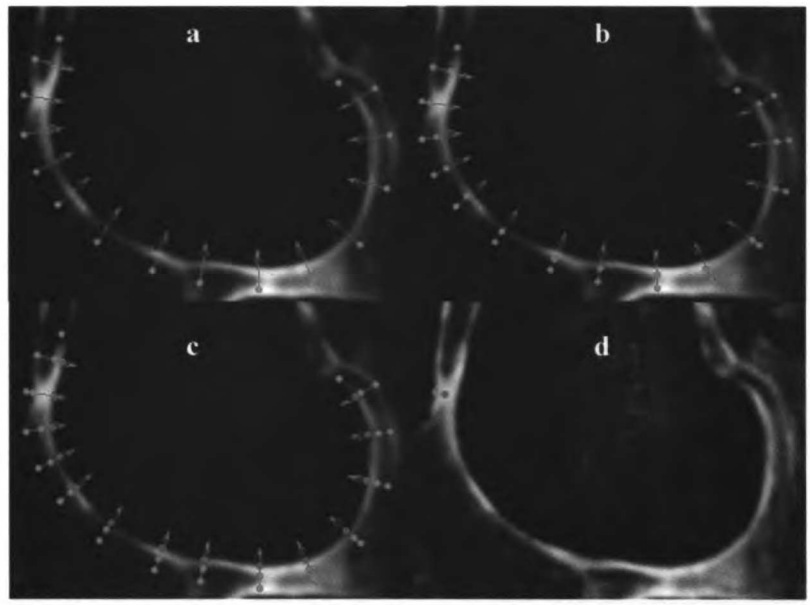

Fig. 3.5. (a) Line profiles used to find the articular surface are shown with magenta arrows. (b) Red points representing the articular surface at the line profiles. (c) Green points representing the bone-cartilage interface at the line profiles. (d) Cyan point gives an alternative position for the red point which was considered to be far away from the bone-cartilage interface. Note the different image pre-processing in (c) and (d).

The rationale of finding two possible positions for each edge was the implementation of an automatic technique that tried to detect and correct thick cartilage sections as those that could occur in the patello-femoral and tibio-femoral articulations where the edges are not always well defined. This correction was focused on the articular surface since computed edges at the bone- cartilage interface were considered more reliable. So the mean distance between all corresponding articular and bone edge points was found, and any pair of points under the process described in the previous paragraph (Fig. 3.5c) that was above this value was flagged. So, with more pairs of points contributing to create the average thickness threshold, the technique was more robust.

Then for each articular point of a flagged pair, a new edge was searched in the first half of the line profile towards the bone. This edge was the last peak of the first derivative of brightness of the line profile. Fig. 3.5d shows with a cyan point the new articular position for the red point, which for this example was the only found to be fixed. If no peaks were found, the points were not displaced from their current articular edges. For this thickness correction step, the original sub-image was taken again and processed with an anisotropic diffusion algorithm (λ=0.25, *number of iterations*=10, K=5) followed by contrast enhancement with a power law transformation (c=1, γ=2).

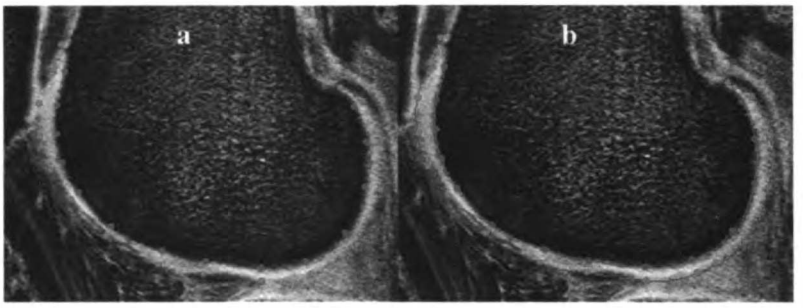

Fig. 3.6. (a) Points in green and red showing the final bone-cartilage interface and articular surfaces for the corresponding initial control points of the spline in Fig. 3.4a. (b) Final Bezier splines defining the bone-cartilage interface (green) and articular surface (red) were created based on control points of (a).

So the first bone-cartilage interface points that were detected remained as the final bone-cartilage points. And the last articular surface points that were detected, were corrected if necessary, and selected as the final articular surface points (Fig. 3.6a). Based on the found edges, new Bezier splines were created to represent the bone-cartilage interface and the articular surface (Fig. 3.6b), giving also an automatic labeling for posterior use in the thickness calculation.

If cartilage happened to be disconnected, a Bezier spline was positioned inside of each cartilage component as is shown in Fig. 3.7a. In order to segment a contiguous slice, only the corresponding end points for each Bezier spline were needed (Fig. 3.7c) doing

the segmentation based on information from the previously segmented slice (Fig. 3.7b and Fig. 3.7c). At any moment the user was able to manually adjust not satisfactory point positions.

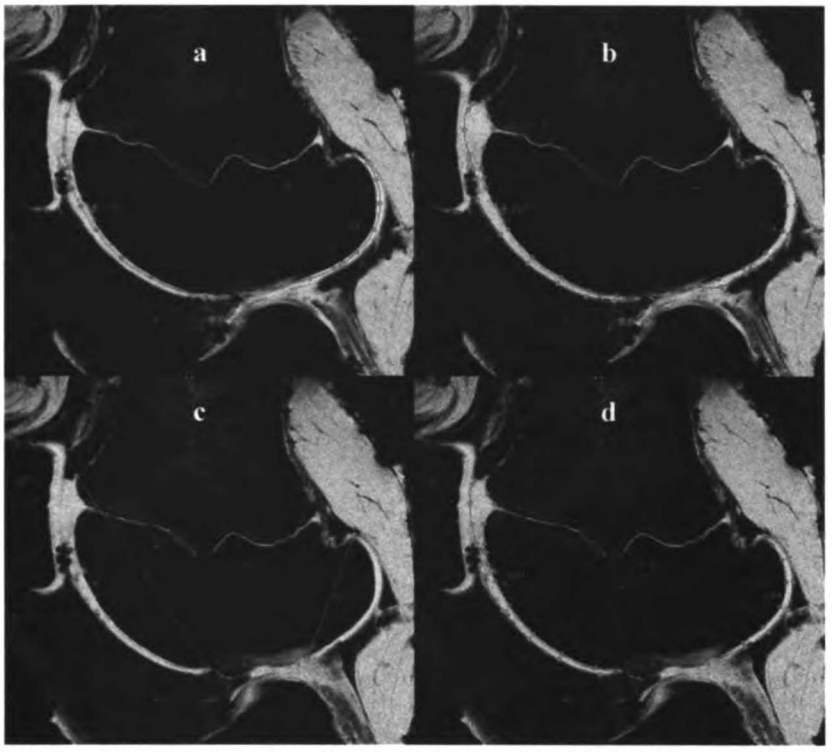

Fig. 3.7. Segmentation of porcine femoral cartilage at 3T. (a) Initial segmentation splines. One spline per cartilage segment is required. (b) Final segmentation of (a) after manual adjustment in the thick region of the patello-femoral articulation. (c) Initial segmentation splines of contiguous slice. Only the end points of each spline are required (splines of 2 points). (d) Final segmentation of (c) based on initial guess from (b), and after manual adjustment in the thick region of the patello-femoral articulation.

References.

[1] S.K. Warfield, M. Kaus, F. A. Jolesz, R. Kikinis, "Adaptive, template moderated, spatially varying statistical classification," *Medical Image Analysis*, 4 (2000) 43-45.

[2] S. Ghosh, O. Beuf, D.C. Newitt, M. Ries, N. Lane and S. Majumdar, "Watershed Segmentation of High Resolution Articular Cartilage Images for Assessment of OsteoArthritis," *Proceedings ISMRM*, 2000.

[3] J. A. Lynch, S. Zaim, J. Zhao, A. Stork, C. G. Peterfy, H. K. Genant. "Cartilage segmentation of 3D MRI scans of the osteoarthritic knee combining user knowledge and active contours," *Proceedings SPIE*, 2000.

[4] T. Stammberger, F. Eckstein, M. Michaelis, K. Englmeier, M. Reiser, "Interobserver Reproducibility of Quantitative Cartilage Measurements: Comparison of B-Spline Snakes and Manual Segmentation," *Magnetic Resonance Imaging*, vol. 17, no. 7, pp. 1033-1042, 1999.

[5] Z. A. Cohen, D. M. McCarthy, S. D. Kwak, P. Legrand, F. Fogarasi, E. J. Ciaccio, and G. A. Ateshian, "Knee cartilage topography, thickness, and contact areas from MRI: in vitro calibration and in-vivo measurement," *Osteoarthritis and Cartilage*, (1999) 7, 95-109.

[6] J. Carballido-Gamio, T. C. Dunn, G. Lau, S. Banerjee, and S. Majumdar, "Evaluation of a semi-automatic segmentation of cartilage based on K-means," *Proceedings ISMRM*, 2003.

[7] J. Carballido-Gamio, K-Y Lee, and S. Majumdar, "MRI cartilage of the knee: segmentation, analysis, and visualization," *Proceedings ISMRM*, 2004.

[8] J.S. Bauer, C. Ross, X. Li, J. Carballido, S.Banerjee, R. Krug, E. Ozhinsky, S. Majumdar, T.M. Link, " Optimization and Reproducibility Evaluation of Volumetric Cartilage Measurements of the Knee at 1.5T and 3T," *Proceedings ISMRM*, 2005.

[9] E. Ozhinsky and S. Majumdar, "3D Visualization of Cartilage Thickness in Knee Joint Using Bezier Spline Segmentation," *Proceedings ISMRM*, 2003.

[10] T.C. Dunn TC, Y. Lu , H. Jin, M.D. Ries, S. Majumdar, "T2 relaxation time of cartilage at MR imaging: comparison with severity of knee osteoarthritis," *Radiology*, vol. 232, no. 2, pp. 592-598, 2004.

[11] K.Y. Lee, T.C. Dunn, L.S. Steinbach, E. Ozhinsky, M.D. Ries, S. Majumdar, "Computer-aided quantification of focal cartilage lesions of osteoarthritic knee using MRI," *Magnetic Resonance Imaging*, vol. 22, no. 8, pp. 1105-1115, 2004.

[12] G. Blumenkrantz, C.T. Lindsey, T.C. Dunn, H. Jin, M.D. Ries, T.M. Link, L.S. Steinbach, S. Majumdar, "A pilot, two-year longitudinal study of the interrelationship between trabecular bone and articular cartilage in the osteoarthritic knee," *Osteoarthritis and Cartilage*, Dec;12 (12), pp. 997-1005, 2004.

[13] Wald LL, Carvajal L, Moyher SE, Nelson SJ, Grant PE, Barkovich AJ, et al. "Phased array detectors and an automated intensity-correction algorithm for high resolution MR imaging of the human brain". *Magn Reson Med* 1995;34(3):433-9.

[14] P. Perona, T. Shiota, and J. Malik, "Anisotropic diffusion," in *Geometry-Driven Diffusion in Computer Vision*, vol. 1., pp. 73-92, 1994.

[15] R.C. Gonzalez, R.E. Woods, "Digital Image Processing," *Prentice Hall*, 2nd edition, pp 80-84.

Chapter 4
Cartilage interpolation

Because the spatial through-plane resolution (i.e. slice thickness) is commonly coarser than the in-plane resolution in MR acquisitions of the knee, proper interpolation should be performed before 3D analysis of the segmented cartilage. Gray-level and shape-based interpolation are the two main interpolation categories and different papers have been published to approach this common problem in image analysis and display [1-11]. The current technique that is considered the standard for cartilage interpolation is that proposed in [12]. This technique interpolates shape based only on distance fields (DFs), can handle branching, and its robustness has been demonstrated. The interpolation technique presented in this work is a morphing technique, which is a shape-based interpolation method based on DFs and warping [11, 13-16]. The main reason behind this election was that morphing is better to handle situations of objects with heavy invaginations [11] that can occur in cases such as cartilage lesions.

After cartilage was segmented using the semi-automatic technique described in Chapter 3, the labeled contours were used to interpolate its shape to create isotropic voxels. This interpolation was computed using morphing with DFs and warping. However, for the porcine knees at 3T the interpolation was also computed with the standard method based on DFs for comparison purposes. Since in the interpolation process the labeling of the surfaces as bone-cartilage and articular is lost for the interpolated slices, and the labeling is required to compute the 3D cartilage thickness, interpolated surfaces were labeled automatically based on the end points of the splines defining the cartilage segments.

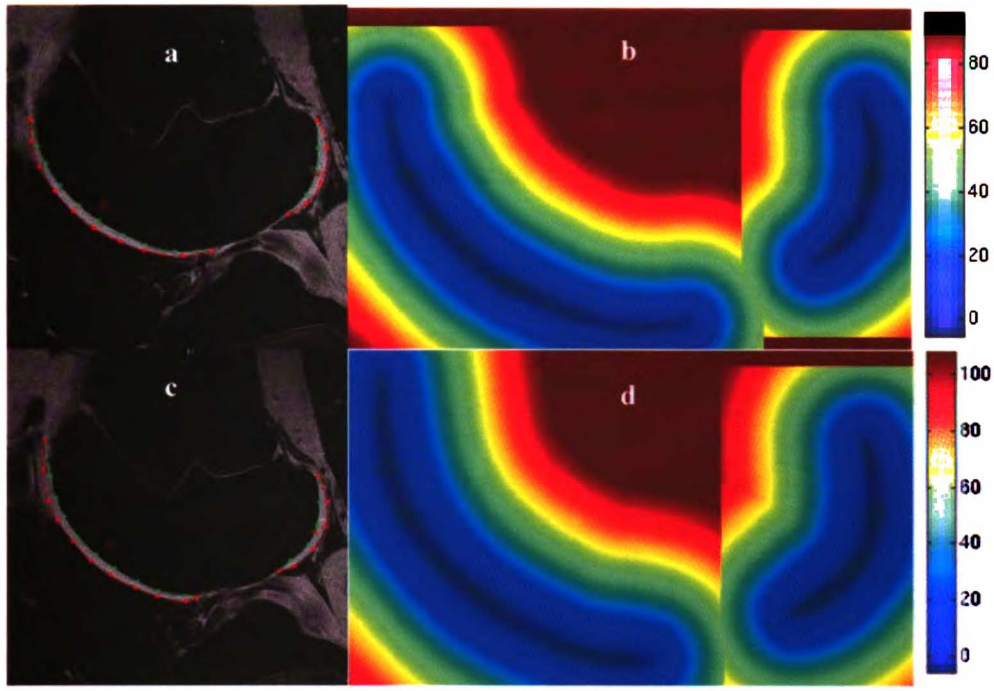

Fig. 4.1. (a) Segmentation of femoral cartilage of a pig knee at slice *n*. (b) Distance map corresponding to the segmentation in (a). (c) Segmentation of femoral cartilage of the same pig knee in (a) at slice *n+1*. (d) Distance map corresponding to the segmentation in (c). Scales in the distance maps are in pixels.

4.1 Distance field shape-based interpolation.

Since the idea was to create a volume with isotropic voxels (or quasi-isotropic) representing the shape of the cartilage, the highest in plane resolution in mm (in the event of non-square pixels) was taken as the desired increment in *z*, which was called *delta z*:

$$delta\ z = min(resolution\ in\ x\ in\ mm,\ resolution\ in\ y\ in\ mm), \quad (4.1)$$

where *min* is the minimum function.

For each segmented slice the Bezier splines representing the bone-cartilage and articular surfaces were evaluated and then discretized. For each contour representing a cartilage segment (disconnected cartilage segments can appear on patients with osteoarthritis (OA) or porcine knees in the same slice) the corresponding minimum and maximum *x* and *y* coordinates of the splines were used to create a bounding box with an

extra frame of 50 pixels (for future interpolation purposes) to speed up the interpolation process. Then for each sub-image I_m (i.e. for each cartilage segment) a distance field DF_m was computed using [17], where the value of each pixel p was computed according to (4.2):

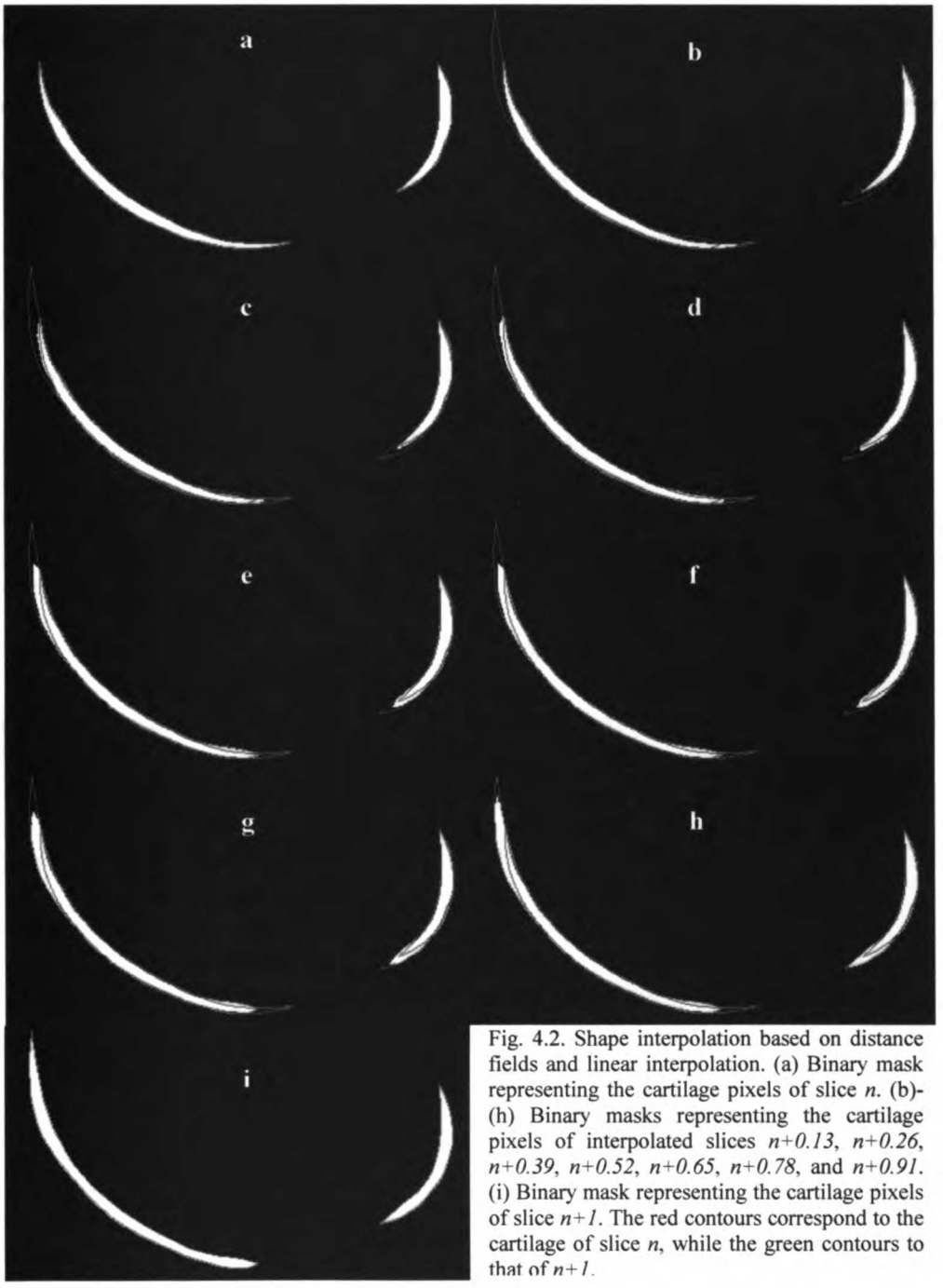

Fig. 4.2. Shape interpolation based on distance fields and linear interpolation. (a) Binary mask representing the cartilage pixels of slice *n*. (b)-(h) Binary masks representing the cartilage pixels of interpolated slices *n+0.13*, *n+0.26*, *n+0.39*, *n+0.52*, *n+0.65*, *n+0.78*, and *n+0.91*. (i) Binary mask representing the cartilage pixels of slice *n+1*. The red contours correspond to the cartilage of slice *n*, while the green contours to that of *n+1*.

$$DF_m(p) = \begin{cases} -dist(p, C_m) & if\ p \in C_m \\ dist(p, C_m) & otherwise, \end{cases}, \tag{4.2}$$

where C_m represents the contour of the cartilage segment m (i.e. the cartilage contour in the sub-image I_m) and *dist* is the Euclidean distance function. After the computation of all the DFs, they were put together in an image of the original size using a minimum operation in case of overlapping of the individual bounding boxes, and a new global bounding box with an extra frame of 20 pixels was created based on the minimum and maximum x and y coordinates of all the splines. Fig. 4.1 shows two examples of femoral cartilage distance maps of porcine knees together with their corresponding cartilage contours overlayed on the original MR image. The examples shown in Fig. 4.1 correspond to contiguous slices: Fig.4.1a is slice n and Fig. 4.1c is slice $n+1$.

So starting from the first segmented slice, the corresponding distance maps of consecutive slices were taken to create new ones at steps of *delta z* mm. The interpolated DFs were created using linear interpolation:

$$DF_{n+t} = (1-t) * DF_n + t * DF_{n+1}, \tag{4.3}$$

where DF_n represents the DF at slice n, DF_{n+1} the DF at slice $n+1$, DF_{n+t} the DF at slice $n+t$, and t is a variable that can take values in the range of [0, 1]. Then, the new interpolated shapes of cartilage were obtained by using (4.4):

$$cart_{n+t} = \{p | DF_{n+t}(p) \le 0\}, \tag{4.4}$$

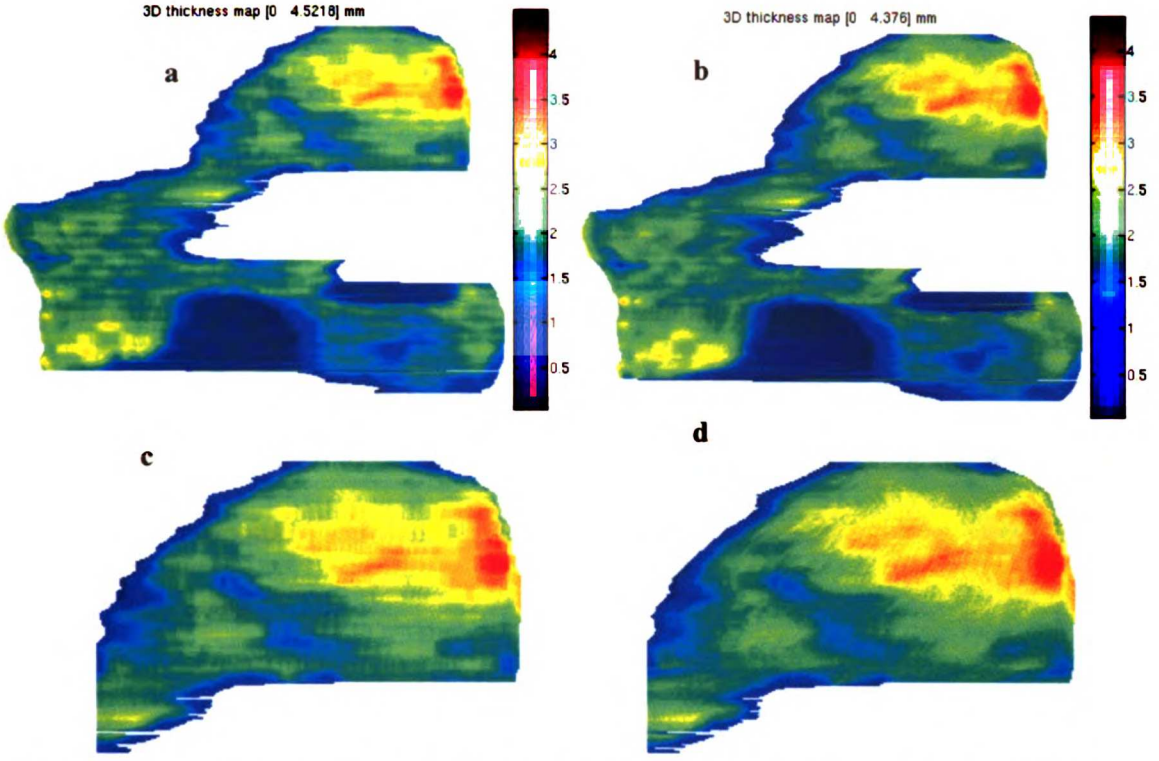

Fig. 4.3. (a) Femoral cartilage thickness map of a porcine knee computed using the interpolated volume based on distance fields. (b) Femoral cartilage thickness map of the same porcine knee in (a) computed using the interpolated volume based on morphing. (c) Zoom of lateral compartment of (a). (d) Zoom of lateral compartment of (b). Note in (b) the slight improvement of removing slice discontinuities with respect to (a). For a more drastic example in a human knee please refer to Fig. 5.1.

where $cart_{n+t}$ represents the set of pixels p inside or in the border of the interpolated cartilage at slice $n+t$. Fig. 4.2 shows the interpolation results accomplished with shape-based interpolation using DFs and linear interpolation for the images shown in Fig.4.1. Fig. 4.3a shows an example of a femoral cartilage thickness map of a porcine knee computed using the interpolated volume based on distance fields and linear interpolation.

4.2 Morphing

The interpolation of cartilage shape based on a morphing technique also required the computation of DFs. This computation was done exactly in the same way as described in section 4.1 by using (4.1) and (4.2).

All the splines representing the cartilage contours were modified so that the number of points at the evaluation time was proportional to the perimeter of the cartilage. From the pair of contiguous segmented slices under evaluation, the slice with more disconnected cartilage segments was selected, and each modified contour was matched to a cartilage segment of the other slice based on minimum Euclidean distances. Then based on the relative positions to the end points, an artificial matching of at least *20* points was done as shown in Fig. 4.4 to obtain corresponding landmarks at slices n and $n+1$. In order to find the interpolated cartilage at slice $n+t$, linear interpolation was applied to the landmarks by using (4.5):

$$L_{n+t} = (1-t) * L_n + t * L_{n+1}, \tag{4.5}$$

where L_n represents the set of landmarks at slice n, L_{n+1} the set of landmarks at slice $n+1$, L_{n+t} the set of landmarks at slice $n+t$, and t is a variable that can take values in the range of [0, 1].

Fig. 4.4. (a) Artificial point matching of slice n (red) and slice $n+1$ (green). Corresponding points are indicated with small circles and connected with blue vectors. (b) Zoom of right segment of (a).

Using the radial basis functions with compact support described in [18] and [19], the warping parameters were computed to elastically register the set of landmarks L_{n+t}

(source) to the set of landmarks L_n (target 0) and L_{n+1} (target 1). The computed registration parameters were then applied to the coordinates of the image containing the landmarks L_{n+t}, and by using bilinear interpolation two new DFs were obtained: DF_0' (for target 0) and DF_1' (for target 1). Using linear interpolation the interpolated distance field DF_{n+t} was computed by using (4.6) and the pixels representing the interpolated shape of cartilage were obtained by using (4.4):

$$DF_{n+t} = (1-t) * DF_0' + t * DF_1'. \tag{4.6}$$

Fig. 4.5 shows the interpolation results accomplished with shape-based interpolation using the morphing technique for the images shown in Fig.4.1. Fig. 4.3b shows an example of a femoral cartilage thickness map of a pig knee computed using the interpolated volume based on the technique just described.

4.3 Labeling of cartilage surfaces

Labeling of the cartilage surfaces as bone-cartilage interface and articular surface is required for the computation of 3D cartilage thickness measurements using either 3D minimum Euclidean distances or a normal vector approach. Unfortunately this information is lost for the interpolated slices in the two shape-based interpolation techniques just described. So, an automatic labeling technique was developed.

Since the splines defining the segmented cartilage were drawn in a predefined order (see Chapter 3 for more details), the first point of the first spline, and the last point of the last spline were taken for both contiguous slices under evaluation. Using linear interpolation the positions of these points for the slice $n+t$ were computed to obtain:

$$f_{n+t} = (1-t) * f_n + t * f_{n+1} \tag{4.7}$$

$$l_{n+t} = (1-t) * l_n + t * l_{n+1}. \tag{4.8}$$

In (4.7) f_{n+t} represents the first point of the first spline in slice $n+t$, and same idea applies to f_n and f_{n+1}. In (4.8) l_{n+t} represents the last point of the last spline in slice $n+t$, and same idea applies to l_n and l_{n+1}.

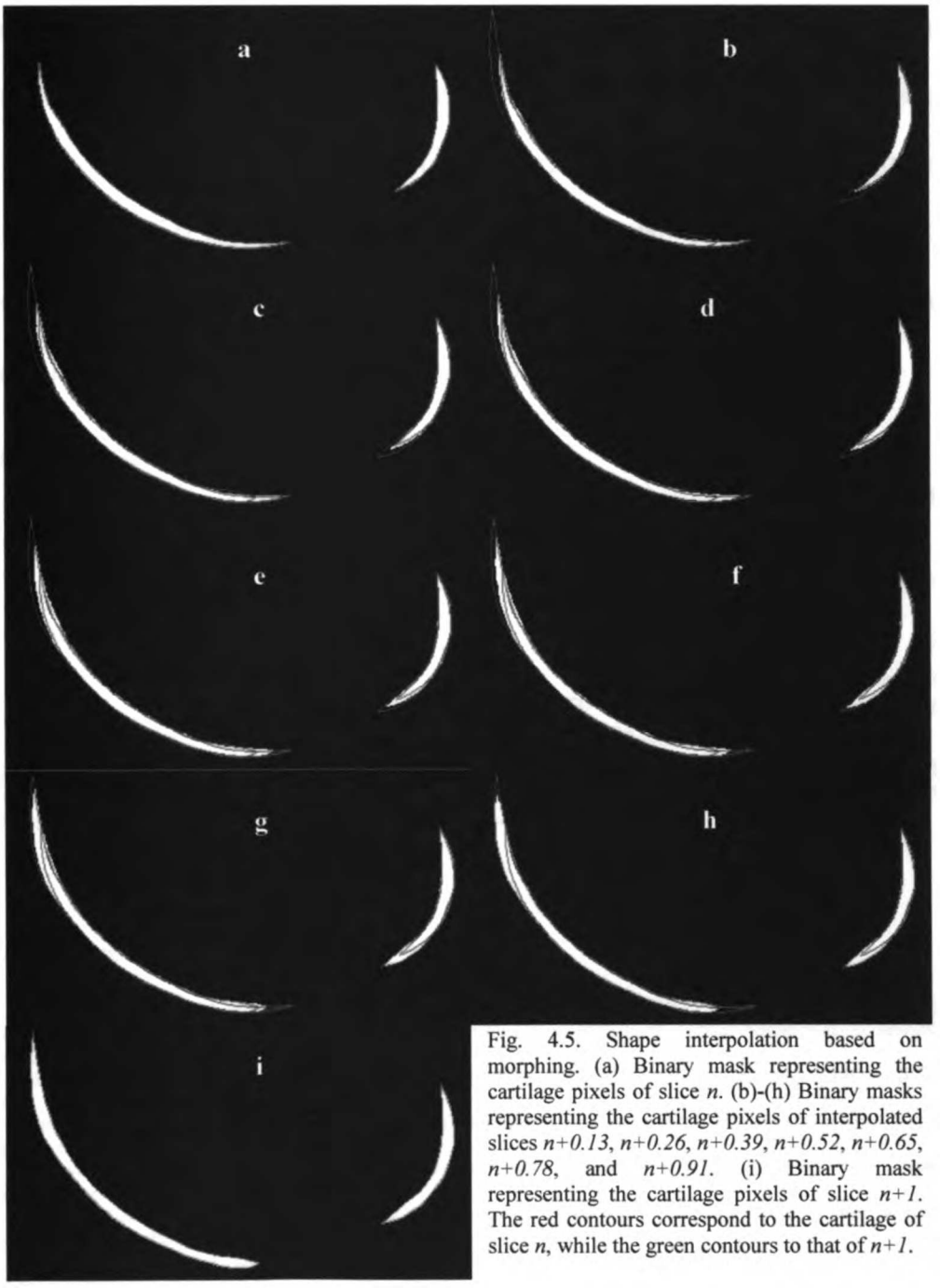

Fig. 4.5. Shape interpolation based on morphing. (a) Binary mask representing the cartilage pixels of slice *n*. (b)-(h) Binary masks representing the cartilage pixels of interpolated slices *n+0.13*, *n+0.26*, *n+0.39*, *n+0.52*, *n+0.65*, *n+0.78*, and *n+0.91*. (i) Binary mask representing the cartilage pixels of slice *n+1*. The red contours correspond to the cartilage of slice *n*, while the green contours to that of *n+1*.

For f_{n+t} the closest pixel in $cart_{n+t}$ was found and assigned as the starting point for both the bone-cartilage and articular surfaces (Fig. 4.6a). For l_{n+t} the closest pixel in $cart_{n+t}$ was found and assigned as the last point for both the bone-cartilage and articular surfaces (Fig. 4.6b). If $cart_{n+t}$ contained disconnected cartilage segments, the closest pixel to the first cartilage segment was assigned as the starting point of the second cartilage segment. Using the same rationale, the remaining first points of the cartilage segments were found. The remaining last points of cartilage segments were found in a similar way starting from the last cartilage segment. Fig. 4.6 shows two labeling examples for new interpolated slices, as well as pictorial representation of what is called first cartilage segment, last cartilage segment, first point, last point, etc.

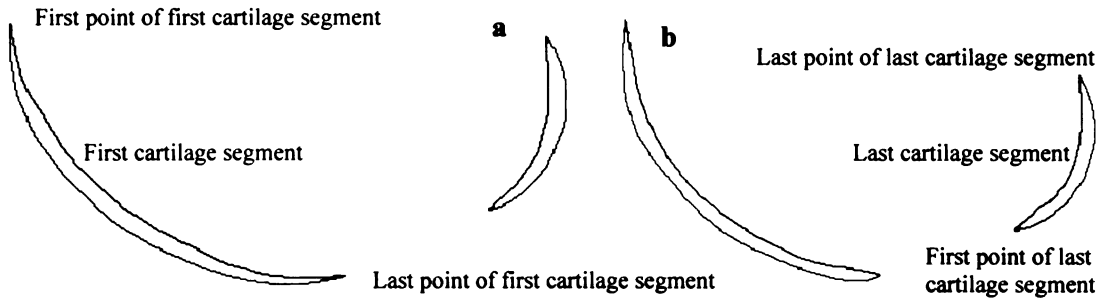

Fig. 4.6. (a) Labeling of interpolated femoral cartilage of a pig knee at slice $n+0.13$. (b) Labeling of interpolated femoral cartilage of same pig knee as in (a) at slice $n+0.91$. Cyan lines represent the bone-cartilage interface, while the magenta ones represent the articular surface.

References.

[1] D. Levin, "Multidimensional Reconstruction by Set-valued Approximation," *IMA J. Numerical Analysis*, 6:173-184, 1986.

[2] S.P. Raya and J. K. Udupa, "Shape-Based Interpolation of Multidimensional Objects," *IEEE Transactions on Medical Imaging*, vol. 9, no. 1, March 1990.

[3] G. T. Herman, J. Zheng, C. A. Bucholtz, "Shape-based interpolation," IEEE *Computer Graphics and Applications* 12(3):69-79, 1992.

[4] J.-F. Guo, Y.-L. Cai, and Y.-P. Wang, "Morphology-based interpolation for 3D medical image reconslruction," *Cornput. Meal. Imaging Graph.*, vol. 19, no. 3, pp. 267 279, 1995.

[5] G. J. Grevera, J. K. Udupa. "Shape-Based Interpolation of Multidimensional Grey-Level Images," *IEEE Transactions on Medical Imaging*, vol. 15, no. 6, December 1996.

[6] B. Migeon, R. Charreyron, P. Deforge, P. Marché, "Improvement of morphology-based interpolation," *Proceedings of the 20th Annual International Conference of the IEEE EMBS*, vol. 20, no. 2, 1998.

[7] B. Migeon, R. Charreyron, P. Deforge, A. Langlet, J. Renard, P. Marche, "An automatic spline-based contour interpolation for the 3D reconstruction of a thin walled elastic tube," *Journal of Biomechanics* 31 (1001) (1998) pp. 70-70.

[8] Tong-Yee Lee and Wen-Hsiu Wang. "Morphology-Based Three-Dimensional Interpolation," *IEEE Transactions on Medical Imaging*, vol. 19, no. 7, July 2000.

[9] Vassilios Chatzis and Ioannis Pitas. "Interpolation of 3-D Binary Images Based on Morphological Skeletonization," *IEEE Transactions on Medical Imagining*, vol. 19, no. 7, July 2000.
[10] A. G. Bors, L. Kechagias, and I. Pitas. "Binary Morphological Shape-Based Interpolation Applied to 3-D Tooth Reconstruction," *IEEE Transactions on Medical Imaging*, vol. 21, no. 2, February 2002.
[11] Tong-Yee Lee and Chao-Hung Lin. "Feature-Guided Shape-Based Image Interpolation," *IEEE Transactions on Medical Imaging*, vol. 21, no. 12, December 2002.
[12] T. Stammberger, F. Eckstein, K. Englmeier, M. Reiser, "Determination of 3D Cartilage Thickness Data From MR Imaging: Computational Method and Reproducibility in the Living," *Magnetic Resonance in Medicine*, 41:529-536(1999).
[13] T. Beier, and S. Neely, "Feature-Based Image Metamorphosis," *Computer Graphics*, 26, 2, July 1992.
[14] D. Cohen-Or, D. Levin, A. Solomovici, "Contour Blending Using Warp-Guided Distance Field Interpolation," *Proc. IEEE Visualization*, 1996.
[15] H. Johan, Y. Koiso, T. Nishita, "Morphing Using Curves and Shape Interpolation Techniques," *Proc. Pacific Graphics*, 2000.
[16] D. Cohen-Or, D. Levin, A. Solomovici, "Three-Dimensional Distance Field Metamorphosis," *ACM Transactions on Graphics*, vol. 17, no. 2, pp. 116-141, 1998.
[17] H. Breu, J. Gil, D. Kirkpatrick, and M. Werman, "Linear Time Euclidean Distance Transform Algorithms,"*IEEE Trans. PAMI*, vol. 17, no. 5, pp. 529-533, May 1995.
[18] H. Wendland, "Piecewise polynomial, positive definite and compactly supported radial basis functions of minimal degree," *Adv. Comput. Math.*, vol. 4, pp. 389-396, 1995.
[19] M. Fornefett, K. Rohr, H.S. Stiehl, "Radial basis functions with compact support for elastic registration of medical images," *Image and Vision Computing*, 19, pp. 87-96, 2001.

Chapter 5
Cartilage thickness

Different morphological, molecular, and biochemical biomarkers for predicting or evaluating the degree of osteoarthritis (OA) of the knee have been investigated [1]. Thickness and volume are the morphological biomarkers that have received more attention since thinning of cartilage is a common manifestation of this pathology.

Quantification of cartilage thickness based on MR images of the knee requires proper 3D image processing techniques. The limited slice resolution compared to the in-plane resolution results in highly anisotropic voxels that make the depicted cartilage dependent on patient positioning and slice orientation among other factors. After cartilage segmentation has been performed (see Chapter 3 for more details) the common approach to perform 3D cartilage thickness measurements has consisted of a two step process:

1. Computation of isotropic voxels (see Chapter 4 for more details).
2. Computation of 3D cartilage thickness.

The objective of the first step is to obtain cartilage surfaces that are independent of patient positioning or slice orientation.

To complete the second step different techniques have been proposed in the literature to perform cartilage thickness measurements [2-4]. However there are only two real 3D techniques that are equivalent although their approaches are different: normal vector approach and minimum Euclidean distance method.

The normal vector approach consists in computing distances normal to the articular surface or to the bone-cartilage interface. The distance normal to the articular surface refers to the length of the vector normal to the articular surface and ending at the bone-

cartilage interface, and same reasoning for the distance normal to the bone-cartilage interface.

The minimum Euclidean distance approach consists in finding for each point in a surface the closest one in the opposite.

In this work after cartilage segmentation, shape-based interpolation to create isotropic voxels, and corresponding labeling of cartilage surfaces as bone-cartilage interface and articular surfaces, for each point on the articular surface the closest point on the bone-cartilage interface was found and the corresponding distance was assigned as its thickness value. This technique is equivalent to find the distances normal to the bone-cartilage interface but avoids the explicit calculation of normal vectors [3]. The directionality of this computation was chosen based on [5] where Lösh et al demonstrated that this method is superior for the delineation of focal cartilage lesions.

For validation purposes thickness measurements were done for three different cases for the porcine knees at 3T:

1. Cartilage with no shape interpolation (anisotropic resolution).
2. Cartilage with shape interpolation using only DFs (isotropic resolution).
3. Cartilage with shape interpolation using the morphing technique (isotropic resolution).

Fig. 5.1a, 5.1b, and 5.1c show examples of 3D femoral cartilage thickness maps of a human knee for these 3 different cases, respectively.

Visualization of quantitative data offers additional advantages to characterize the cartilage morphology. Using MATLAB image processing toolbox rendering of the common 3D color coded thickness maps was possible as is shown in Fig. 5.1. However, a

new way to visualize 3D cartilage thickness in a slice by slice basis with color coding overlaid on the MR images was also developed as is shown in Fig. 5.1d.

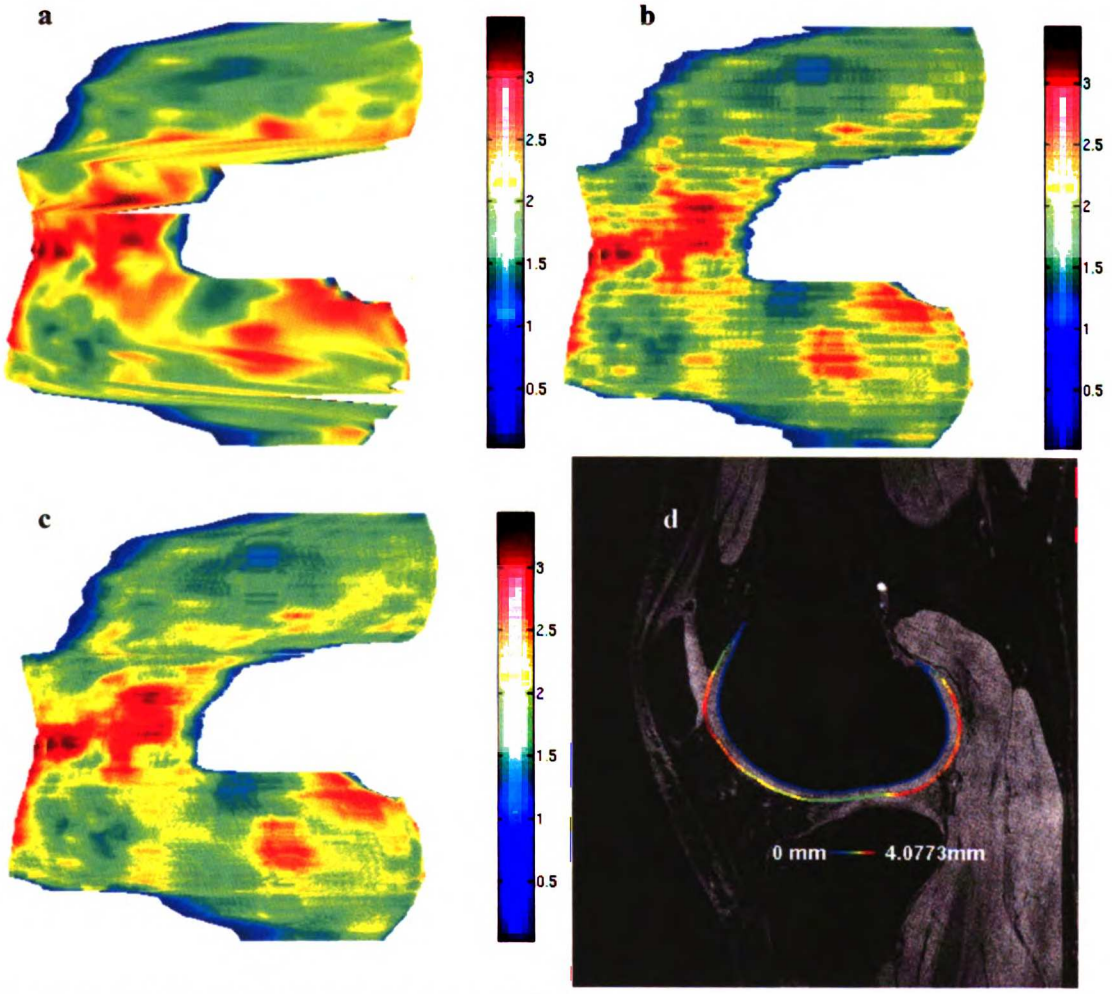

Fig. 5.1. Visualization of cartilage thickness maps. (a) Femoral cartilage thickness map of a human knee with no prior shape interpolation. (b) Femoral cartilage thickness map of the same human knee of (a) with prior shape interpolation using distance fields. (c) Femoral cartilage thickness map of the same human knee of (a) with prior shape interpolation using the morphing technique. (c) Visualization of 3D cartilage thickness information overlaid on the MR image. Scale bars are in mm.

References

[1] M. L. Gray, F. Eckstein, C. Peterfy, L. Dahlberg, Y-J Kim, and A.G. Sorensen, "Toward Imaging Biomarkers for Osteoarthritis," *Clinical Orthopaedics and Related Research*, 2004, Number 427S, pp. S175–S181.

[2] Z. A. Cohen, D. M. McCarthy, S. D. Kwak, P. Legrand, F. Fogarasi, E. J. Ciaccio, and G. A. Ateshian, "Knee cartilage topography, thickness, and contact areas from MRI: in vitro calibration and in-vivo measurement," *Osteoarthritis and Cartilage*, (1999) 7, 95-109.

[3] T. Stammberger, F. Eckstein, K. Englmeier, M. Reiser, "Determination of 3D Cartilage Thickness Data From MR Imaging: Computational Method and Reproducibility in the Living," *Magnetic Resonance in Medicine*, 41:529-536(1999).

[4] A.A. Kshirsagar, P.J. Watson, J.A. Tyler, L.D. Hall, "Measurement of Localized Cartilage Volume and Thickness of Human Knee Joints by Computer Analysis of 3D MR Images," *Invest. Radiol.*, vol. 33, no. 5, pp. 288-99, 1999.

[5] A. Lösch, F. Eckstein, M. Haubner, K-H Englmeier. "A non-invasive technique for 3-dimensional assessment of articular cartilage thickness based on MRI—Part I: Development of a computational method,".Magn Reson Imaging 1997;15:795–804.

Chapter 6
Cartilage volume

As was mentioned in Chapter 5, cartilage volume and thickness are the morphological properties of knee cartilage that have been more investigated in the search of a biomarker for characterization of osteoarthritis (OA) of the knee [1]. Computation of cartilage volume is more straightforward than thickness; however the requirement of isotropic voxels should still be valid. As for cartilage thickness, volume measurements were done for three different cases for the porcine knees at 3T for validation purposes:

1. Cartilage with no shape interpolation (anisotropic resolution).
2. Cartilage with shape interpolation using DFs (isotropic resolution).
3. Cartilage with shape interpolation using the morphing technique (isotropic resolution).

Also for validation purposes for the porcine knees at 3T the volume was digitally computed with two different methods:

1. Counting the number of voxels inside and on the cartilage contours.
2. Counting the number of voxels inside and on the cartilage contours with different weightings according to predefined patterns of voxels [2] (see Appendix A).

For the porcine knees at 1.5T the volume was only digitally computed for the cartilage interpolated with the morphing technique (see Chapter 4 for more details) and by using the first digital volumetric method.

To validate the segmentation and morphing techniques, the femoral cartilage of all porcine knees was scraped off and its volume was measured using a water displacement method after image acquisition [3].

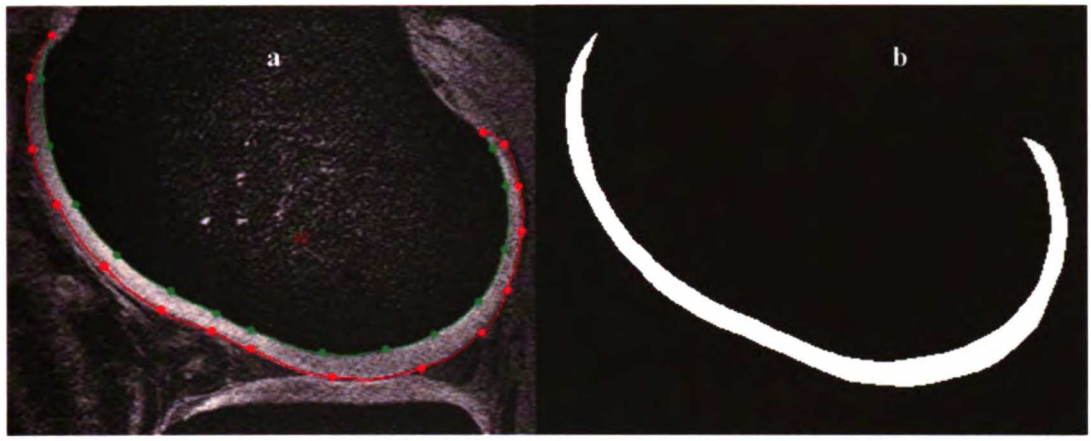

Fig. 6.1. (a) Femoral cartilage segmentation of a human knee. (b) Binary image representing only cartilage voxels of (a). These voxels are then used to compute cartilage volume.

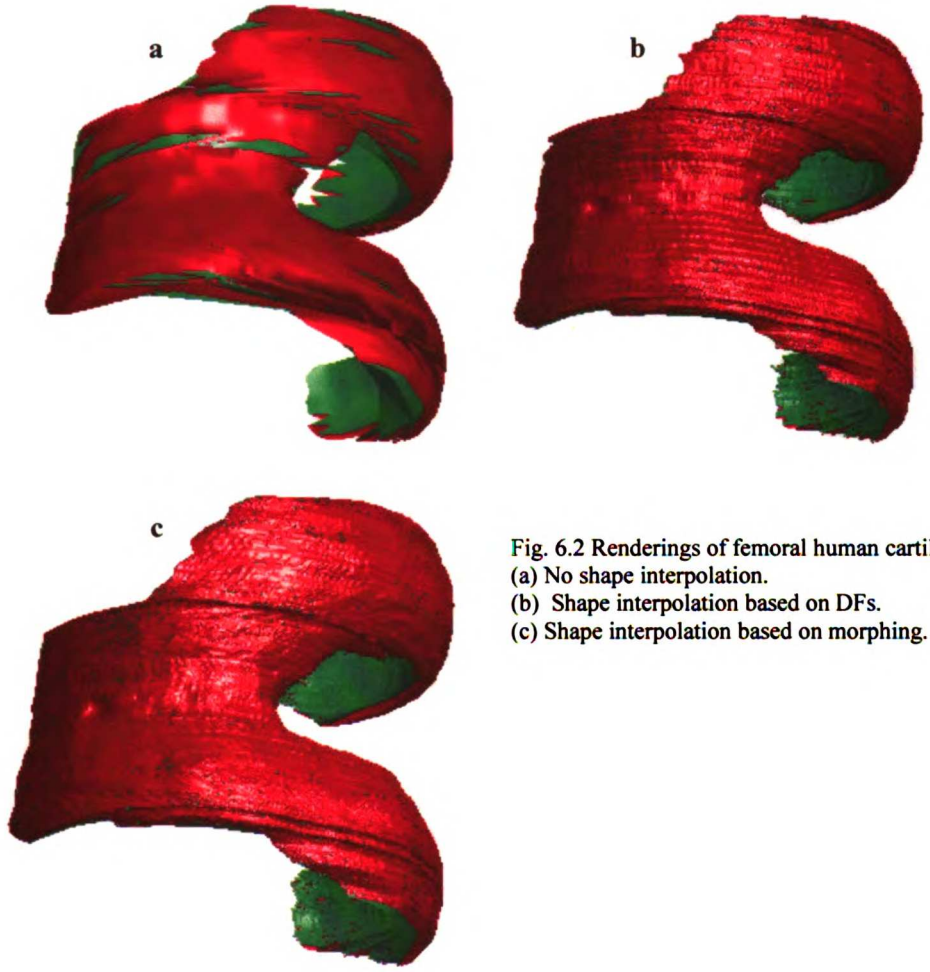

Fig. 6.2 Renderings of femoral human cartilage.
(a) No shape interpolation.
(b) Shape interpolation based on DFs.
(c) Shape interpolation based on morphing.

Fig. 6.1 shows representative images used in the digital process of computing cartilage volume, while Fig. 6.2 shows corresponding renderings of knee cartilage of a human knee with no shape interpolation (a), shape interpolation based on DFs (b), and shape interpolation based on morphing (c).

References

[1] M. L. Gray, F. Eckstein, C. Peterfy, L. Dahlberg, Y-J Kim, and A.G. Sorensen, "Toward Imaging Biomarkers for Osteoarthritis," *Clinical Orthopaedics and Related Research*, 2004, Number 427S, pp. S175–S181.

[2] W.K. Pratt, "Digital Image Processing," John Wiley & Sons, Inc., pp. 634, 1991.

[3] J.S. Bauer, S. Krause, C.J. Ross, R. Krug, J. Carballido-Gamio, E. Ozhinsky, S. Majumdar, and T.M. Link, "Reproducibility and Accuracy Evaluation of Volumetric Cartilage Measurements of the Knee at 1.5T and 3T," *Submitted.*

Chapter 7
Registration of cartilage surfaces

In follow-up studies where MR images of the knee of the same subject are obtained at different time points, image registration is necessary for comparisons of corresponding cartilage points. Different intra-subject registration techniques have been proposed for this purpose [1-5]. However, if a comparison involves two different subjects at any time, inter-subject registration should be addressed. Few publications have approached the inter-subject registration for comparisons of cartilage of the knee [6-8]. In [6] Dardzinski et al proposed a 2D technique for inter-subject comparison of MR T2 relaxation times. In [7] Slavinsky et al proposed a 3D affine transformation which was followed by a set of 2D elastic registrations using manually identified landmarks to compare maps of cartilage thickness. And in [8], which is the only 3D technique, the authors used a bone statistical shape model to obtain corresponding regions of knee articular cartilage. In this work semi-automatic (since segmentation requires interaction) rigid-body (intra-subject) and elastic (inter-subject) registration techniques are proposed, where the alignment of cartilage surfaces is based on the registration of the corresponding bone structures instead of using the cartilage surfaces themselves, which gives robustness to the technique especially with patients affected by osteoarthritis (OA) where cartilage shapes can drastically change from subject to subject. These registrations allow the comparison of cartilage characteristics point to point. The technique uses shape matching based on 3D shape-contexts [9-11] (see Chapter 2 for additional information) to establish corresponding landmarks between the segmented bones to be registered. By using these landmarks the solution to the absolute orientation problem proposed in [12] is used for the rigid-body/affine transformation followed by the elastic registration using

Wendland's radial basis functions (RBFs) with compact support [13-14] if inter-subject registration is required. Once the registration parameters are computed, these are applied to the corresponding source cartilage surface (e.g. femoral cartilage if femoral registration is performed) and then a point to point correspondence to the target cartilage surface is done using minimum Euclidean distances.

7.1 Segmentation of bone structures

Bones were segmented from MR images using a semi-automatic technique as in the cartilage segmentation. This technique was based on Bezier splines and edge detection as was described in Chapter 3. The user placed control points close to the bone-cartilage interface following its shape to create a Bezier spline (Fig. 7.1 a). The spline was placed counter-clockwise (with the center of the clock in the corresponding bone). Then, based on the minimum and maximum x and y coordinates of the splines, a bounding box with an extra frame of 30 pixels was created to speed up the segmentation process, and the new sub-image was normalized against its maximum gray level value. The bone edges were then enhanced using an anisotropic diffusion algorithm [15] (λ=0.25, *number of iterations*=5, K=90) and a median filter (7 pixels x 7 pixels), followed by a contrast enhancement technique based on a power law transformation [16] (c=1, γ=1/3). Then rays perpendicular to the spline on the control points were traced towards the bone to a distance equal to a width of 15 pixels. From these positions, line profiles were computed back to the edge of the bone using bicubic interpolation with an average of two points per pixel (Fig. 7.1b) for a total of 60 points (~30 pixels). After computing the first derivative of brightness of the line profiles, the maximum value was taken as the edge of the bone for each point (Fig. 7.1b and Fig. 7.1c). Based on the found edges, a new Bezier

spline was created to represent the bone shape as is shown in Fig. 7.1d. The control points of this spline were then copied to the next slice to perform the corresponding segmentation assuming a smooth transition of shape from slice to slice. At any moment the user had the opportunity to manually adjust no satisfactory end positions.

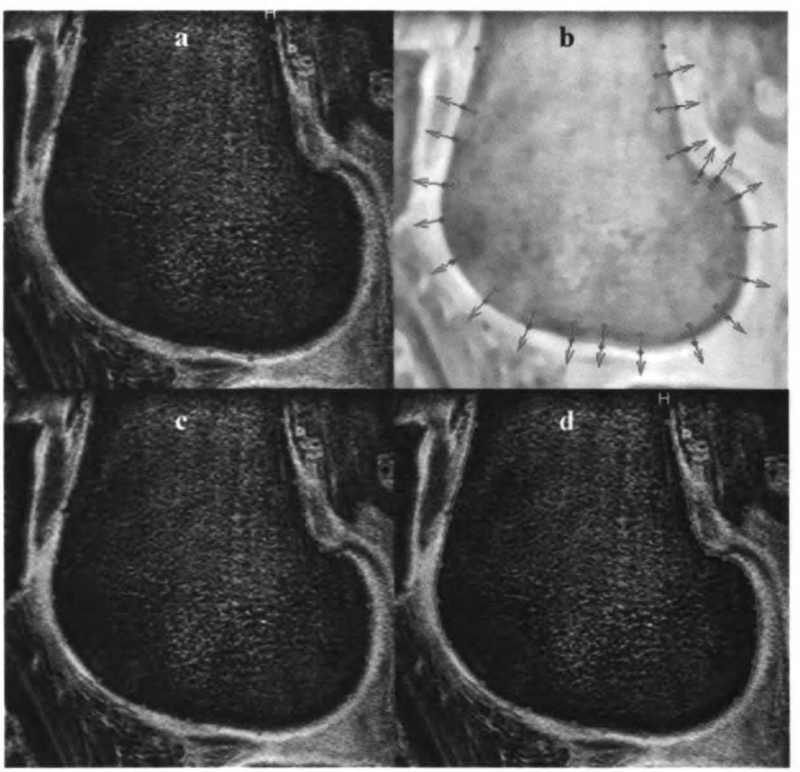

Fig. 7.1. (a) Initial spline defining the shape of a human femur is shown in green with its corresponding control points for a human knee. (b) Line profiles used to find the bone edges are shown with red arrows, while green points represent the bone edges at the line profiles on a pre-processed image. (c) Same green points as in (b) overlaid on the original image. (d) Bezier spline created with the control points in (c) representing the final bone segmentation.

7.2 Point matching using three dimensional *shape-contexts*

After the segmentation of the source and target bones was accomplished, corresponding points in the two shapes were automatically detected using 3D shape shape-contexts [9-11]. Splines representing the source and target bone shapes were evaluated then discretized and uniformly sampled (every 13 pixels). For each pixel in

these sampled contours a histogram representing the point distribution of the relative remaining points was computed. The bins were uniform in a 3D log-polar space (r, θ [0, 2π) and φ [0, π]) to make the 3D shape-contexts more sensitive to nearby points than to those far away.

All shape-contexts were made scale invariant by normalizing the radial distances by the mean distance of all the pair-wise distances in the shape [9].

Since shape-contexts are not rotational invariant when computed using an absolute frame, further processing had to be completed. The solution suggested in [9] to satisfy this criterion in 2D was to find the tangent vector at each point and use it as the positive x-axis to compute the shape-contexts. Instead of computing 3D normals at each point, our approach took advantage of the valid assumptions that the bones to be registered were similar in shape especially at their mid-slices, that rotation is minimal due to the knee holder used during MRI acquisition, and that shape-contexts are insensitive to small perturbations [9]. So the discretized edges of the mid-slices of the segmented bones were taken, and 2D rotational invariant shape-contexts were computed for both mid-slices (7 values for r starting at 1/8, and 18 values for θ equally distributed in the range [0 2π)) followed by the corresponding point matching (at least 70% of the target points were matched) as is shown in Fig. 7.2a. Based on this matching the source slice was rigidly aligned in 3D to the target slice with a rotation matrix calculated by using the closed form solution presented in [12]. This 3D rotation matrix was then applied to all the slices of the source shape to have approximately the same initial orientation for the two bones before 3D shape-context computation.

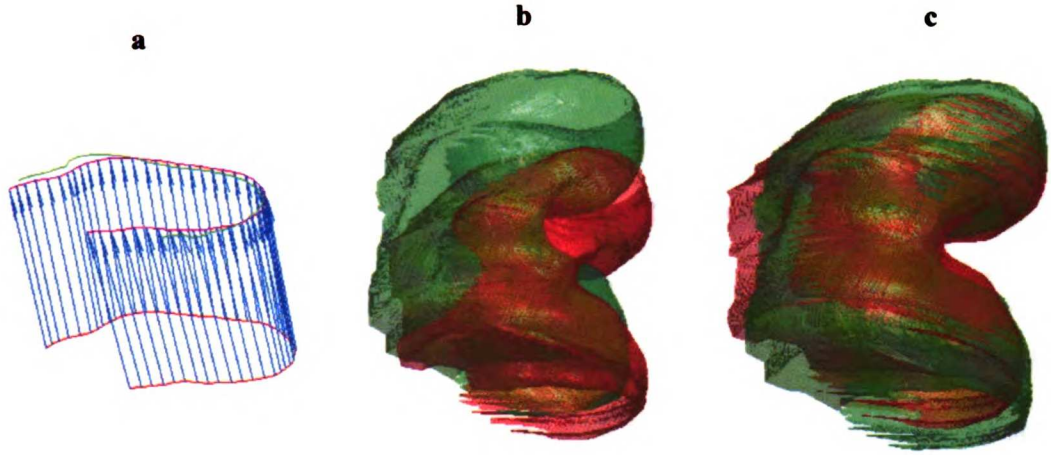

Fig. 7.2. Human femoral inter-subject registration. (a) Matching of mid-source (red) and mid-target (green) slices. The magenta line represents the source slice after rotation, scaling, and translation based on the 2D rotational invariant matching. (b) Original source (red) and target (green) femurs. (c) Source (red) and target (green) femurs after affine registration (rotation, scaling, and translation).

In order to match two shapes (2D or 3D) their corresponding shape-contexts were compared to each other based on the χ^2 test statistic (7.1), a simple and effective measure of histogram similarity [17-18]:

$$\chi^2(h_i, h_j) = \frac{1}{2}\sum_{k=1}^{K}\frac{(h_i(k) - h_j(k))^2}{h_i(k) + h_j(k)}, \tag{7.1}$$

Once all the pair-wise costs were computed, the optimal point matching was solved by using COPAP [19].

In order to match only a fraction of points, equation (7.2) was followed:

$$min\_landmarks = f * min\ (n_S, n_T), \tag{7.2}$$

where f is a constant in the range [0, 1], n_S is the number of points representing the source shape, n_T the number of points representing the target shape, and *min* is the minimum function. For the initial 2D matching, f was 0.7, n_S was the number of points representing the source mid-slice, and n_T was the number of points representing the target mid-slice.

7.3 Intra-subject registration

Intra-subject registration was accomplished through affine registration. After the initial rough alignment proposed in Section 7.2 based on the mid-slices of the source and target bones, 3D shape-contexts were computed for both source and target shapes. The histogram bins were uniform in 3D log-polar space: r [1/8, rmax], θ [0, 2π) and φ [0, π]; and seven values for each variable were used in this work for a total of 7^3 (343) bins. A total of *30* shape-contexts were uniformly selected from the first to the last point defining the edges of the target shape, the cost matrix was then computed by using (7.1), and the 3D point matching by using COPAP. For (7.2) f was 0.8, n_T was 30, and n_S was equal to the number of points representing the 3D source shape. By using the set of corresponding points given by COPAP, the closed-form solution presented in [11] was used to obtain the 3D rotation matrix, scaling, and translation parameters to map the source bone to the target.

After this 3D initial registration, the 3D process described above was repeated with no initial alignment based on the mid-slices and the same 30 uniformly selected target shape-contexts. If only rigid-body registration was required for intra-subject alignment, the cumulative rotations were applied to the source articular cartilage surface. If affine registration was needed, the cumulative rotations were applied together with the scale and translation parameters corresponding to the last alignment. Fig. 7.2b represents an example of a source (red) and target (green) femurs before any registration, while Fig. 7.2c represents the same bones after affine registration.

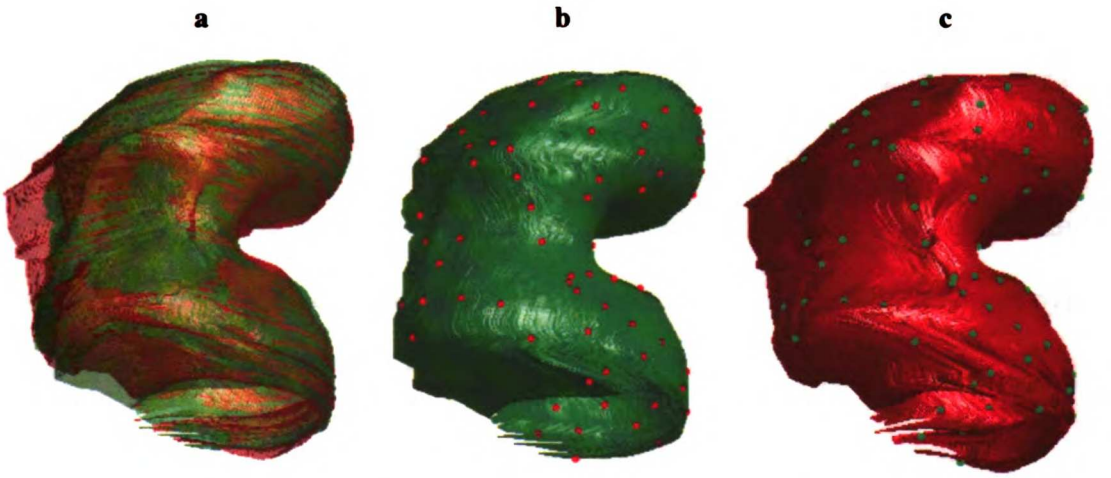

Fig. 7.3. Human femoral inter-subject registration. (a) Source (red) and target (green) femurs after affine (rotation, scaling, and translation) and elastic registration. (b) Target femur is shown in green with the last set of landmarks used for the elastic registration in red. (c) Source femur is shown in red after rigid-body and elastic registration with the last set of landmarks used for the elastic registration in green.

7.4 Inter-subject registration.

Elastic registration was computed after the corresponding affine transformation. Shape-contexts in 3D were computed for both source and target shapes with seven values for each variable r, θ, and φ. A total of 60 shape-contexts were then uniformly selected from the first to the last point defining the edges of the target shape, the cost matrix was computed by using (7.1), and COPAP was again used for the 3D point matching using the following values for (7.2): f=0.8, n_T=60, and n_S was equal to the total number of points representing the 3D source shape. By using the set of corresponding landmarks given by COPAP, the coefficients to perform elastic registration using Wendland's RBFs with compact support were computed and applied to the source bone. This elastic registration step was repeated a second time where the number of shape-contexts of the target shape was increased to 90 (i.e. n_T=90). For both elastic registration steps equation (7.3) was used to calculate the support parameter a as suggested in [14]:

$$a = 1.25*3.66*max(abs(Sland-Tland)), \quad (7.3)$$

where *Sland* is a 3 column array where each row contains the x, y, and z coordinates of a source landmark; *Tland* is also a 3 column array with the corresponding coordinates for the target landmarks; *abs* is the absolute function; and *max* is the maximum function.

Figure 7.3a shows an overlaid of the source and target femurs after rigid-body and elastic registration. The last set of landmarks for the elastic-registration is shown overlaid on the target (Fig. 7.4b) and source bones (Fig. 7.4c).

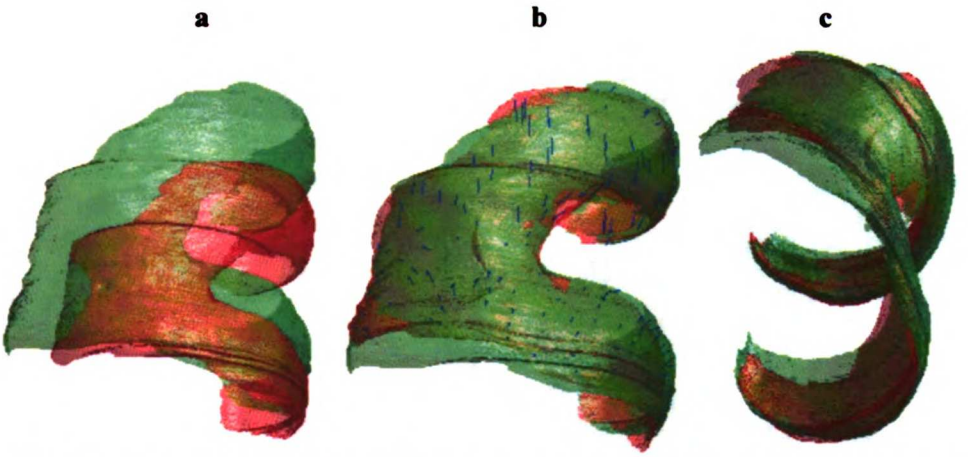

Fig. 7.4. Human femoral inter-subject cartilage registration. (a) Original source (red) and target (green) femoral cartilage surfaces. (b) Source (red) and target (green) femoral cartilage surfaces after affine (rotation, scaling, and translation) and elastic registration. Randomly selected blue vectors are connecting corresponding points of the source and target femoral cartilage surfaces. (c) A different view of (b) with no vectors.

7.5 Cartilage surface matching.

As was previously described in the introduction of this chapter, the registration of cartilage surfaces was accomplished based on the registration of the corresponding bones (e.g. registration of femoral cartilage surfaces, based on the registration of the corresponding femurs) giving robustness to the technique. So the registration parameters

found for the intra- and inter-subject registration of bones were applied to the source cartilage surface as is shown in Fig. 7.4.

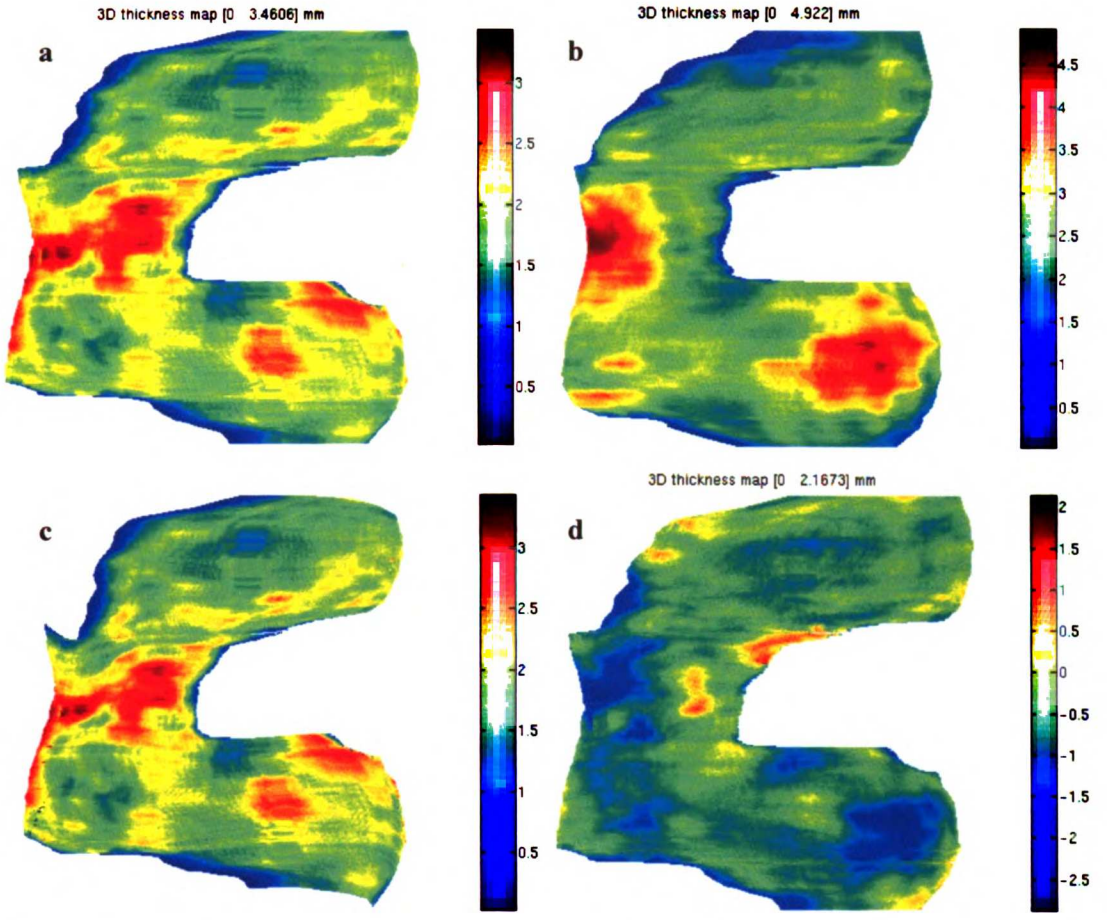

Fig. 7.5. (a) Source femoral cartilage thickness map of subject 1. (b) Target femoral cartilage thickness map of subject 2. (c) Thickness map of (a) after warping to match (b). (d) The result of subtracting (b) from (c) and unwarping. Scale bars are in mm.

Finally, in order to find a one to one point correspondence between the source and target surfaces of cartilage, the surfaces were matched using minimum Euclidean distances.

An example of a possible application of the registration technique just proposed is shown in Fig. 7.5. This example demonstrates the feasibility of comparing femoral

cartilage thickness maps of two subjects point by point. Figure 7.5d is the resulting thickness map after subtracting the target map from the warped map and unwarping the coordinates. In this image regions tending to a blue color (e.g. anterior section of right epicondyle) mean that the source cartilage surface is thinner than the target. And regions tending to a red color mean that the source cartilage surface is thicker than the target (small region between the epicondyles).

It is important to clarify that the cartilage thicknesses were calculated prior to the registration, so their values remained unchanged during the transformation.

References.

[1] Z. A. Cohen, D. M. McCarthy, S. D. Kwak, P. Legrand, F. Fogarasi, E. J. Ciaccio, and G. A. Ateshian, "Knee cartilage topography, thickness, and contact areas from MRI: in vitro calibration and in-vivo measurement," *Osteoarthritis and Cartilage*, (1999) 7, 95-109.

[2] A.A. Kshirsagar, P.J. Watson, J.A. Tyler, L.D. Hall, "Measurement of Localized Cartilage Volume and Thickness of Human Knee Joints by Computer Analysis of 3D MR Images," *Investigative Radiology.*, vol. 33, no. 5, pp. 288-99, 1999.

[3] T. Stammberger, J. Hohe, K-H Englmeier, M. Reiser, F. Eckstein, "Elastic Registration of 3D Cartilage Surfaces from MR Image Data for Detecting Local Changes in Cartilage Thickness," *Magnetic Resonance in Medicine*, 44, pp. 592-601, 2000.

[4] J. A. Lynch, S. Zaim, J. Zhao, C.G. Peterfy, H.K. Genant, "Automating measurement of subtle changes in articular cartilage from MRI of the knee by combining 3D image registration and segmentation," *SPIE Proceedings*, 2001.

[5] C. Kauffmann, P. Gravel, B. Godbout, A. Gravel, G. Beaudoin, J-P Raynauld, J. Martel-Pelletier, J-P Pelletier, and J.A. de Guise, "Computer-Aided Method for Quantification of Cartilage Thickness and Volume Changes Using MRI: Validation Study Using a Synthetic Model," *IEEE Transactions on Biomedical Engineering*, vol. 50, no 8, August 2003.

[6] B.J. Dardzinski, V.J. Schmithorst, T.J. Mosher, M.B. Smith, "Cartilage Warping: A Technique for Inter-Subject Comparison of T2 Relaxation Time," *Proceedings ISMRM*, 2002.

[7] J. P. Slavinsky, E. Ozhinsky, S. Majumdar, "A Combination of Rigid and Elastic Registration Methods for a Standard Atlas of the Knee," *Proc. ISMRM*, 2003.

[8] T.G. Williams, C. J. Taylor, Z-X Gao and J.C. Waterton, "Corresponding Locations of Knee Articular Cartilage Thickness Measurements by Modelling the Underlying Bone," *MIUA 2003, Proc. 7th. Annual Conf. on Medical Image Understanding and Analysis*, 2003.

[9] S. Belongie, J. Malik, and J. Puzicha, "Shape Matching and Object Recognition Using Shape Contexts,"*IEEE Trans.PAMI*, vol. 24, no. 24, 2002.

[10] J. Carballido-Gamio, K-Y Lee, S. Majumdar, "Automatic 3D point matching of segmented images using shape-contexts," *Proceedings ISMRM*, 2005.

[11] A. Frome, D. Huber, R. Kolluri, T. Bülow, and J. Malik, "Recognizing Objects in Range Data Using Regional Point Descriptors," *European Conf. on Computer Vision*, 2004.

[12] B.K.P. Horn, H.M. Hilden, S. Negahdaripour, "Closed-from solution of absolute orientation using orthonormal matrices," *J. Opt. Soc. Am. A.*, vol. 5, no. 7, 1988.

[13] H. Wendland, "Piecewise polynomial, positive definite and compactly supported radial basis functions of minimal degree," Adv. Comput. Math., vol. 4, pp. 389-396, 1995.

[14] M. Fornefett, K. Rohr, H.S. Stiehl, "Radial basis functions with compact support for elastic registration of medical images," *Image and Vision Computing*, 19, pp. 87-96, 2001.

[15] P. Perona, T. Shiota, and J. Malik, "Anisotropic diffusion," in *Geometry-Driven Diffusion in Computer Vision*, vol. 1., pp. 73-92, 1994.

[16] R.C. Gonzalez, R.E. Woods, "Digital Image Processing," *Prentice Hall*, 2nd edition, pp 80-84.

[17] J. Malik, S. Belongie, J. Shi, and T. Leung, "Textons, contours, and regions: Cue combination in image segmentation," *International Conference on Computer Vision*, Corfu, Greece, Sept. 1999.

[18] J. Puzicha, T. Hofmann, and J. Buhmann, "Non-parametric similarity measures for unsupervised texture segmentation and image retrieval," *Proc. IEEE Conf. Computer Vision and Pattern Recognition*, pp. 267–272, 1997.

[19] C. Scott and R. Nowak, "Robust Contour Matching via the Order Preserving Assignment Problem," submitted. Available at:http://www.stat.rice.edu/~cscott/pubs.html. Unpublished.

Chapter 8
Results

8.1 Cartilage volume at 3T

Pearson correlation coefficients of $r = 0.83$ ($p<0.001$) were found for the cartilage volume of 16 porcine knees measured through the water displacement method and the volume obtained with no shape interpolation, shape interpolation of cartilage with distance fields, and shape interpolation of cartilage with morphing. Since no method was perfect, the data was also statistically analyzed using the Bland-Altman method to check for any deviation. The four methods showed good agreement since all data samples were inside of the band of two standard deviations of the difference of the measurements that were compared. The same type of analysis was applied to compare the different digital methodologies to measure cartilage volume yielding correlation coefficients above 0.95 and at most one sample out of the two standard deviations band for the Bland-Altman method. Fig. 8.1 shows a scatter plot of the volumetric measurements computed by the water displacement method and based on the morphed cartilage at 3T, together with the corresponding least squares regression line; Fig. 8.2 shows a Bland-Altman plot demonstrating that the digital volumetric measurement based on the morphed cartilage at 3T is as good as the water displacement method; and Table 8.1 shows the corresponding volumetric measurements for the first digital volumetric methodology described in Chapter 6.

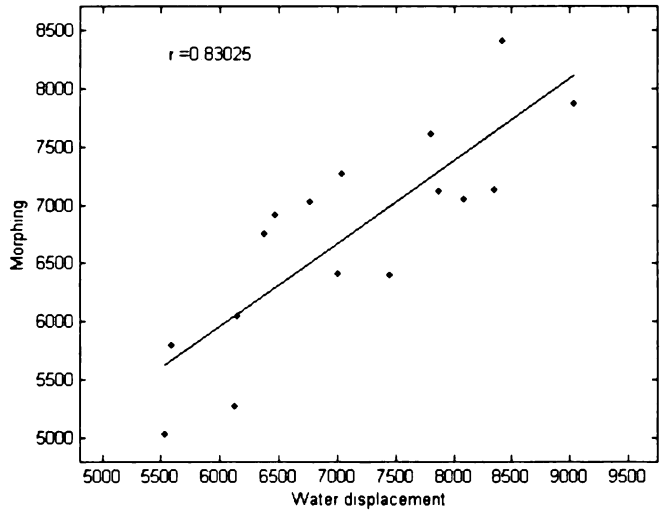

Fig. 8.1 Scatter plot of volumetric measurements (mm^3) computed by the water displacement method and based on the morphed cartilage at 3T. The solid line represents the least squares regression line.

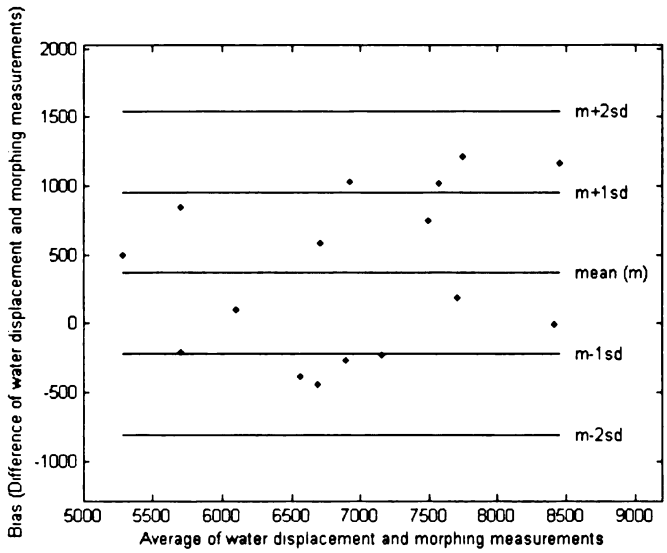

Fig. 8.2 Bland-Altman plot demonstrating that the digital volumetric measurement based on the morphed cartilage at 3T is as good as the water displacement method.

Table 8.1 Results of volumetric measurements (mm^3) of cartilage at 3T.		
Water displacement	Morphed cartilage	Interpolated cartilage using DFs
6150	6048.7	6025.6
5590	5802.3	5830.1
8350	7132.8	7162.8
6120	5271.4	5329.4
7870	7118.2	7164.2
8080	7056.8	7100.8
7000	6415.2	6439.8
7440	6406.9	6431.3
5530	5033.2	5041.8
7040	7273.3	7315.3
7800	7611.0	7650.9
6370	6754.0	6793.1
9030	7868.3	7898.5
8410	8414.9	8437.4
6470	6910.8	6947.1
6760	7032.4	7081.0

8.2 Cartilage volume at 1.5T

A Pearson correlation coefficient r = 0.75 ($p<0.001$) was found for the cartilage volume of 12 porcine knees measured through the water displacement method and the volume obtained with shape interpolation of cartilage with morphing. Since no method was perfect, the data was also statistically analyzed using the Bland-Altman method to check for any deviation. The two methods showed good agreement since all data samples were inside of the band of two standard deviations of the difference of the measurements that were compared. Fig. 8.3 shows a scatter plot of the volumetric measurements computed by the water displacement method and based on the morphed cartilage at 3T, together with the corresponding least squares regression line; Fig. 8.4 shows a Bland-Altman plot demonstrating that the digital volumetric measurement based on the morphed cartilage at 1.5 T is as good as the water displacement method; and Table 8.2 shows the corresponding volumetric measurements.

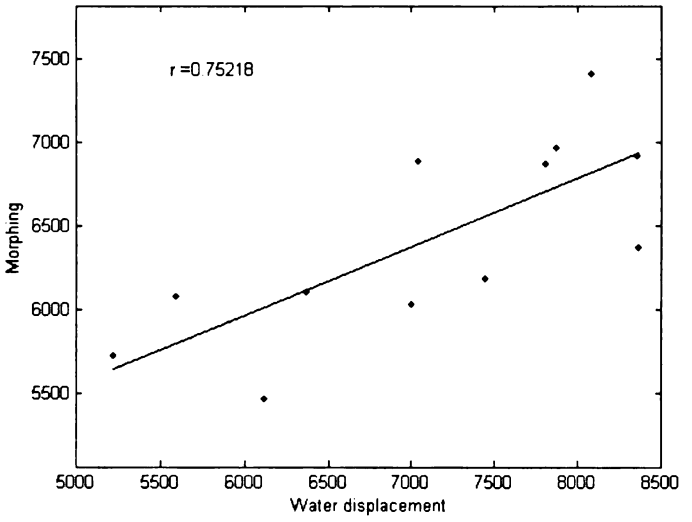

Fig. 8.3 Scatter plot of volumetric measurements (mm^3) computed by the water displacement method and based on the morphed cartilage at 1.5T. The solid line represents the least squares regression line.

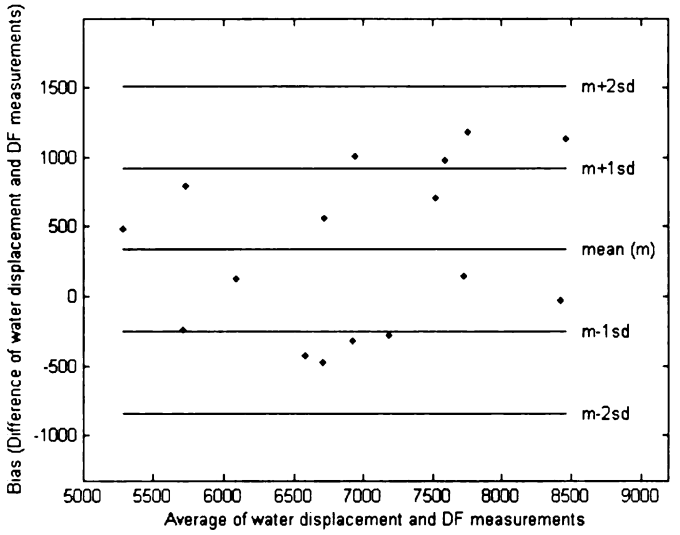

Fig. 8.4 Bland-Altman plot demonstrating that the digital volumetric measurements based on the morphed cartilage at 1.5T is as good as the water displacement method.

Table 8.2 Results of volumetric measurements (mm^3) of cartilage at 1.5T.	
Water displacement method	Morphed cartilage
5590	6081.8
8350	6926.7
6120	5467.3
7870	6973.8
8080	7417.7
7000	6031.8
7440	6189.2
5220	5724.9
7040	6886.7
7800	6876.8
6370	6106.6
8360	6370.9

8.3 Cartilage thickness at 3T

The digital analysis for cartilage thickness at 3T was done as the analysis for cartilage volume at 3T (cartilage with no shape interpolation, cartilage with shape interpolation based on DFs, and cartilage with shape interpolation based on morphing) and similar results were found. Correlation values were above 0.95 ($p<0.001$) and all methods showed good agreement according to the Bland-Altman method. Examples of femoral 3D cartilage thickness maps based on morphed cartilages (see Chapter 4 for more details) are shown in Fig. 8.5a and Fig. 8.5b for a porcine and human knee, respectively.

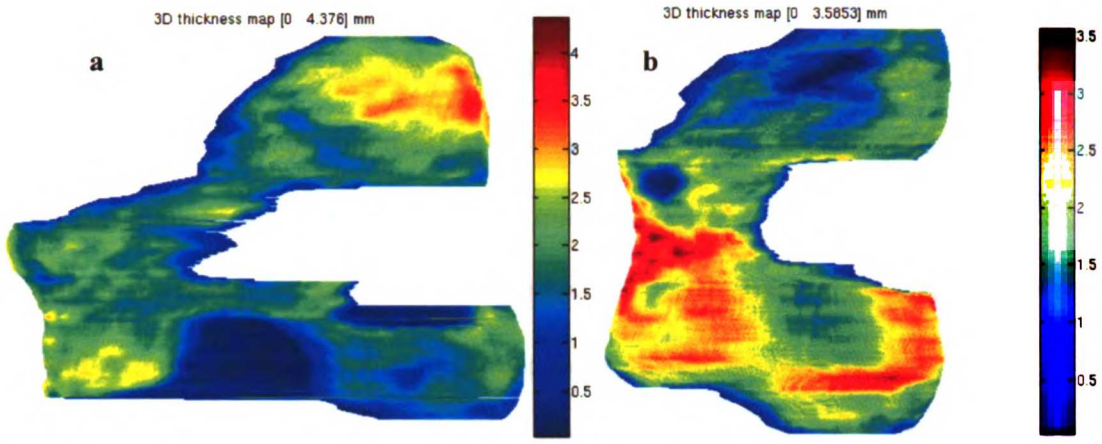

Fig. 8.5 Femoral 3D cartilage thickness maps of a porcine (a) and human (b) knees based on morphed cartilages.

8.4 Shape matching

Tibias manually segmented from sagittal fast spin-echo (FSE)[1] images were borrowed from a parallel study at our institution. In that study the right tibias of the same subjects were registered to the left ones using manual landmarks (approximately 11 landmarks) and Horn's affine approach. Also with the same technique tibias at extension and flexion were registered. Since the registration techniques used in this paper are based on landmarks, and we proposed an automatic technique to establish corresponding landmarks between the source and target shapes, we quantitatively validated the point matching technique using manual registration. The manual approach was statistically compared to the semi-automatic using the Bland-Altman method. The values to be compared were mean Euclidean distances of source and target landmarks after affine registration.

[1] Sagittal fast spin-echo (FSE) images at 1.5T of both knees of 6 different subjects were obtained with in-plane resolution of 0.3125 mm x 0.3125 mm and slice thickness of 1.5 mm. An extra subject was imaged at flexion and extension. Representative images are not shown since they were manually segmented.

The Pearson correlation coefficient for the mean distances of the registered source and target landmarks between the manual and semi-automatic registrations was 0.75 ($p<0.05$, $n=7$) with good agreement according to the Bland-Altman method (Fig. 8.6), and a maximum mean difference of 2.1 mm. However r was 0.9287 for the mean distances of the registered source and target bones, also showing a good agreement with the Bland-Altman method, and a maximum mean difference of 0.45 mm, which is less than the slice thickness (1.5 mm) or 2 pixels (2x0.3125 mm).

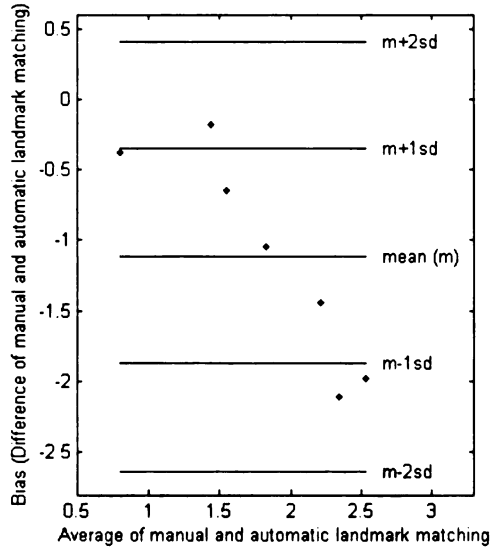

Fig. 8.6 Bland-Altman plot demonstrating that the semi-automatic registration of tibias is as good as the manual technique.

8.5 Inter-subject registration

In addition to the validations previously mentioned, 6 human inter-subject femoral registrations were computed to create difference thickness maps of the source and target femoral cartilage surfaces. The bone segmentations were done with the semi-automatic segmentation technique as described in Chapter 7.

Fig. 8.8 and Fig. 8.9 show two examples (out of 6) of femoral inter-subject cartilage registrations as well as the corresponding difference thickness maps (source minus target)

demonstrating the feasibility of the technique. In the difference maps it is clear that anatomic points are properly being compared (as is also shown in Fig. 7.3 of Chapter 7) between the source and target maps with blue areas representing source thinner cartilage points, while red areas showing thicker points.

Although the difference thickness maps can be displayed in the warped version (Fig. 8.8c and Fig. 8.9c), Fig. 8.8d and Fig. 8.9d show the feasibility of displaying them in the original source coordinates. This is possible because the cartilage thickness maps are calculated before the elastic registration and each point of the articular surface has a thickness value assigned to it.

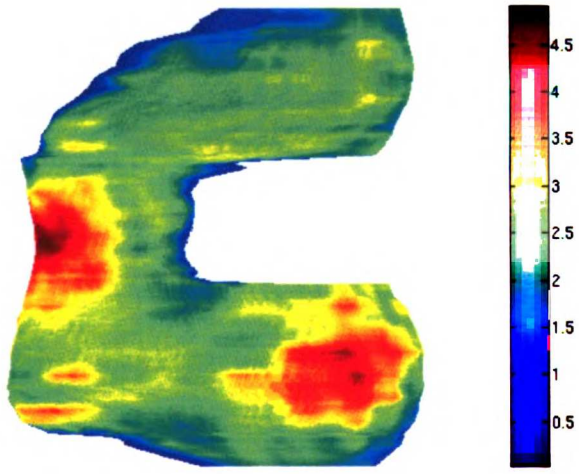

Fig. 8.7 Human femoral 3D cartilage thickness map of a subject with no signs of osteoarthritis (OA0). Scale bar is in mm. Please see Chapter 2 for nomenclature details.

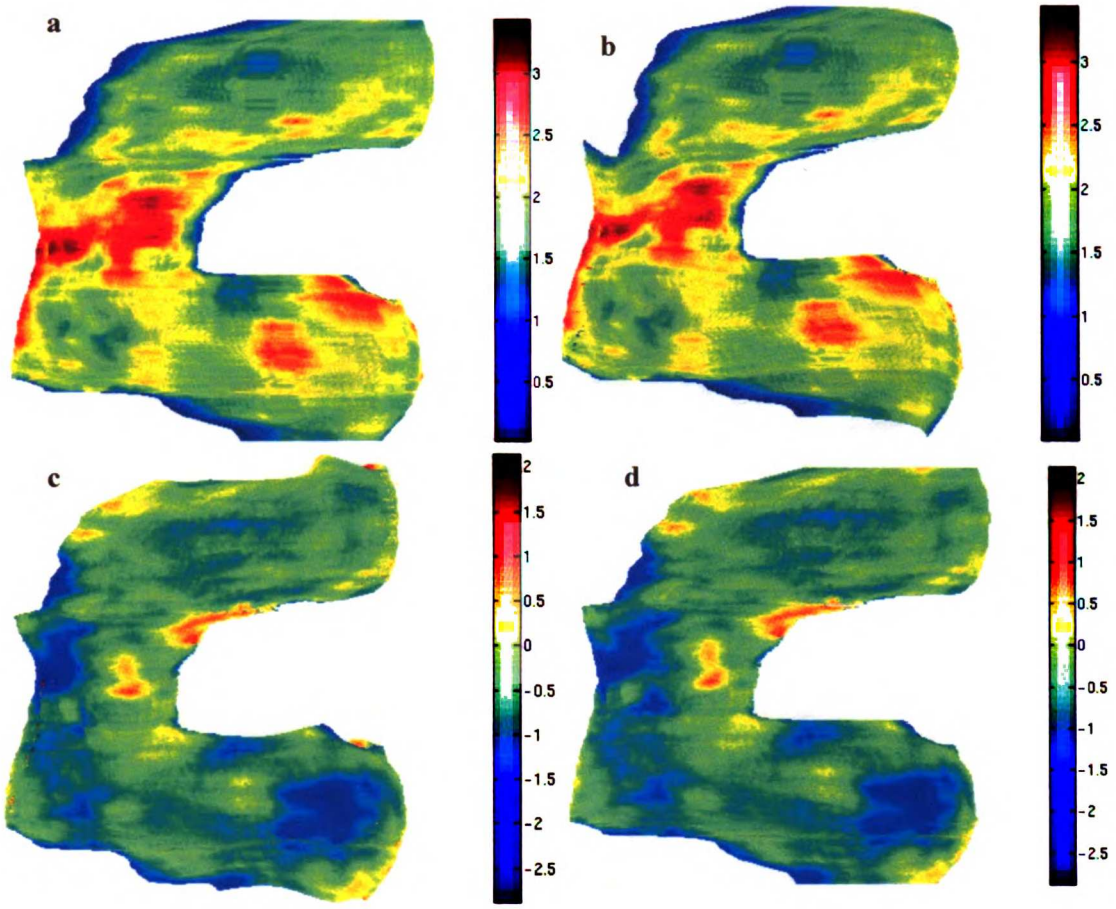

Fig. 8.8 (a) Human femoral 3D cartilage thickness map of an OA1 patient. (b) Thickness map of (a) after elastic registration to Fig. 8.7 based on the corresponding femurs. (c) Difference thickness map after elastic registration and matching: (b) minus Fig. 8.7. (d) Thickness map in (c) after coordinates unwarping. Scale bars are in mm.

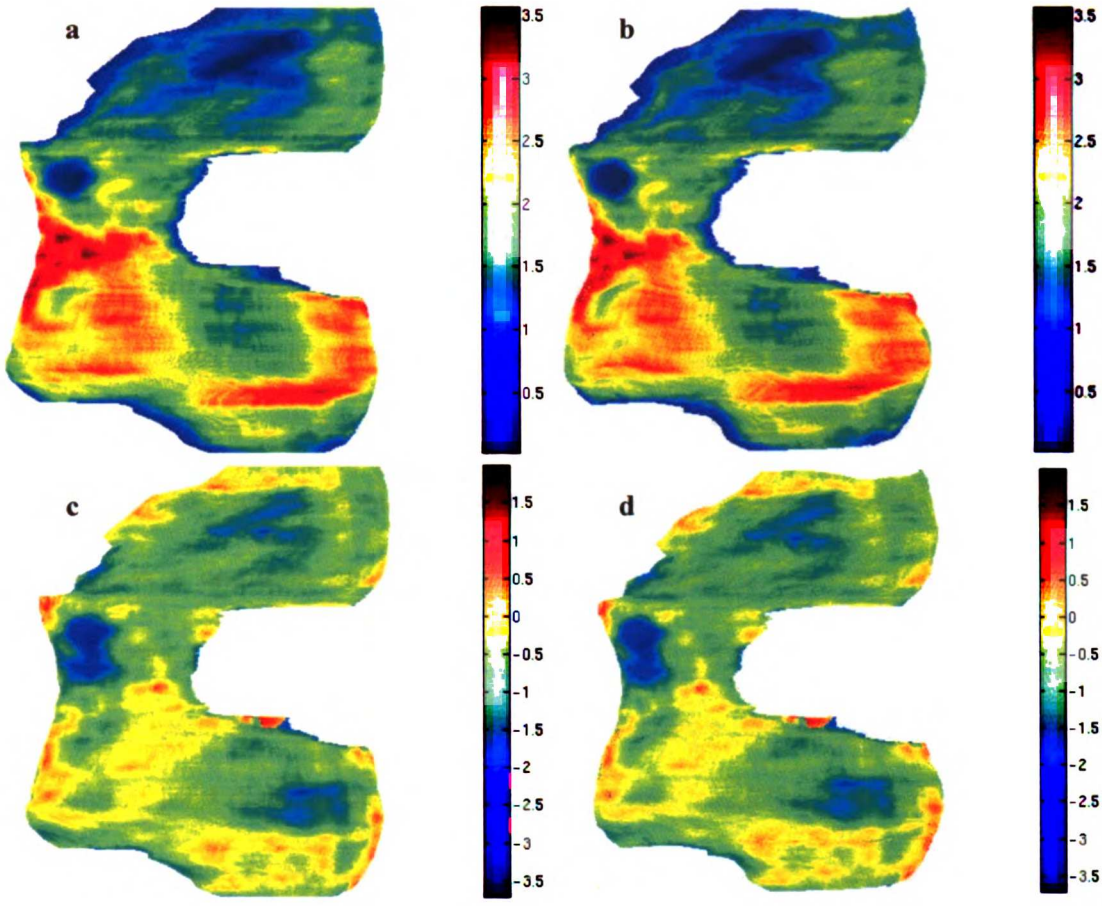

Fig. 8.9 (a) Human femoral 3D cartilage thickness map of an OA2 patient. (b) Thickness map of (a) after elastic registration to Fig. 8.7 based on the corresponding femurs. (c) Difference thickness map after elastic registration and matching: (b) minus Fig. 8.7. (d) Thickness map in (c) after coordinates unwarping. Scale bars are in mm

Chapter 9
Discussion

Osteoarthritis (OA) is the most common form of arthritis in the world and it is a major cause of morbidity in the US and Europe. It is expected that in 2020 59.4 million of Americans will be affected by some form of arthritis [1].

Different morphological, molecular, and biochemical biomarkers for predicting or evaluating the degree of OA of the knee have been investigated [2], being thickness and volume the morphological biomarkers that have received more attention, since thinning of cartilage is a common manifestation of this pathology. MRI in contrast to x-ray imaging allows the visualization and quantification of cartilage morphology. It is important to asses the quantification of knee cartilage morphology to monitor the progression of joint diseases or related treatments, and when this assessment is based on medical images such as MRI, accurate and robust image processing tools are required to perform 3D cartilage quantification and analysis. We have presented and validated a set of techniques to accomplish this goal for the intra and inter-subject analysis.

The segmentation technique proposed in this paper allows the segmentation of about 40 slices in 12 or 15 min with no significant loss of accuracy as it was quantitatively validated with the Bland-Altman method based on volumetric measurements of porcine knees at 1.5T and 3T. With the increase in SNR and contrast between bone and soft tissue structures in MR images of the knee, further or full automation of the segmentation process is still possible. A good candidate technique is Level Set Methods which is a numerical technique that can follow the evolution of interfaces. These interfaces can develop sharp corners, break apart, and merge together [3]

which are essential characteristics to perform cartilage segmentation specially for patients with severe OA.

Volumetric and thickness results could suggest at first glance that there is no need for shape interpolation of cartilage. However, there are certain applications such as analysis and follow-up of focal cartilage lesions where shape interpolation plays a central role. Visual inspection showed that the quality of the cartilage thickness maps was enhanced using the morphing technique for shape interpolation compared to the distance fields (DFs) approach, which in some occasions introduced small artifacts. This improvement however also came with a major computational cost to perform the corresponding point matching and non-elastic registrations (warpings). If shape-interpolation based only on DFs is desired, then cubic interpolation instead of linear would be a better choice.

In follow-up studies, or studies involving different patient populations, proper image processing methods are required to compare common regions or points of cartilage. We have presented and validated a semi-automatic registration technique (since segmentation requires interaction) to accomplish such a goal. The alignment of cartilage surfaces is based on the registration of the corresponding bone structures instead of using the cartilage surfaces themselves, which gives robustness to the technique especially with OA patients where cartilage shapes can drastically change from subject to subject. Since the technique requires the shapes of the bones to perform the alignment, it is still dependent on the segmentations; however the 3D shape-contexts are robust enough to capture corresponding points on the structures of interest as it was statistically demonstrated by the Bland-Altman method using registration based on manual

positioning of landmarks as reference. Using the same reasoning than for cartilage segmentation, the segmentation of bone structures could be automated. The technique of choice for this task would be Statistical Shape Models (see Chapter 2 for more details).

Although the proposed techniques have been applied for comparison of cartilage thicknesses maps, they can also be used to compare other important parameters derived from MRI images such as T1 and T2 relaxation times. Currently it is also in the evaluation process to reduce the manual interaction in a Biomechanics study of the articulation of the knee. If only comparison of anatomic regions is desired (not point to point), 3D shape-contexts could be employed to establish correspondence of common areas with no necessity of elastic registration.

As it was mentioned in Chapter 1, it is important to clarify that the objective of this work was the application and development of image processing techniques to perform intra and inter-subject comparison of knee cartilage morphology rather than deduce any characteristics of cartilage changes during arthritic disease progression.

References.

[1] P. Boulos, A. Papaioannou, K.Beattie and J.D. Adachi, "Measurement Techniques for the Detection of Early Osteoar thritis," *Business briefing:long-term healthcare strategies*, 2003.

[2] M. L. Gray, F. Eckstein, C. Peterfy, L. Dahlberg, Y-J Kim, and A.G. Sorensen, "Toward Imaging Biomarkers for Osteoarthritis," *Clinical Orthopaedics and Related Research*, 2004, Number 427S, pp. S175–S181.

[3] J.A. Sethian, "Level Set Methods and Fast Marching Methods Evolving Interfaces in Computational Geometry, Fluid Mechanics, Computer Vision, and Materials Science," 1999, *Cambridge University Press.*

Appendix A
Digital cartilage volume measurement. Technique 2.

The following is a description of the *bwarea* MATLAB function of the image processing toolbox which was used for the digital computation of cartilage volume (see Chapter 6 for more details).

"*bwarea* estimates the area of all of the on pixels in an image by summing the areas of each pixel in the image. The area of an individual pixel is determined by looking at its 2-by-2 neighborhood. There are six different patterns distinguished, each representing a different area:

3. Patterns with zero on pixels (area = 0)
4. Patterns with one on pixel (area = 1/4)
5. Patterns with two adjacent on pixels (area = 1/2)
6. Patterns with two diagonal on pixels (area = 3/4)
7. Patterns with three on pixels (area = 7/8)
8. Patterns with all four on pixels (area = 1)

Keep in mind that each pixel is part of four different 2-by-2 neighborhoods. This means, for example, that a single on pixel surrounded by off pixels has a total area of 1 [1]."

References

[1] http://www-ccs.ucsd.edu/matlab/toolbox/images/bwarea.html